energies

MDPI

Article

A Comprehensive AC Current Ripple Analysis and Performance Enhancement via Discontinuous PWM in Three-Phase Four-Leg Grid-Connected Inverters

Riccardo Mandrioli, Aleksandr Viatkin, Manel Hammami, Mattia Ricco and Gabriele Grandi *

Department of Electrical, Electronic, and Information Engineering, University of Bologna, 40136 Bologna, Italy; riccardo.mandrioli4@unibo.it (R.M.); aleksandr.viatkin2@unibo.it (A.V.); manel.hammami2@unibo.it (M.H.); mattia.ricco@unibo.it (M.R.)

* Correspondence: gabriele.grandi@unibo.it; Tel.: +39-051-20-93571

Received: 24 July 2020; Accepted: 21 August 2020; Published: 23 August 2020

Abstract: A complete analysis of the ac output current ripple in four-leg voltage source inverters considering multiple modulation schemes is provided. In detail, current ripple envelopes and peak-to-peak profiles have been determined in the whole fundamental period and a comprehensive method providing the current ripple rms has been achieved, all of them as a function of the modulation index. These characteristics have been determined for both phase and neutral currents, considering the most popular common-mode injection schemes. Particular attention has been paid to the performance of discontinuous pulse width modulation (DPWM) methods, including DPWMMAX and DPWMMIN, and their four most popular combinations DPWM0, DPWM1, DPWM2, and DPWM3. Furthermore, a comparison with a few continuous techniques (sinusoidal, centered pulse width modulations, and third harmonic injection) has been provided as well. Moreover, the average switching frequency and switching losses are analyzed, determining which PWM technique ensures minimum output current ripple within the linear modulation range at different assumptions. Numerical simulations and laboratory tests have been conducted to extensively verify all the analytical claims for all the considered PWM injections.

Keywords: inverter; three-phase; current ripple; harmonic distortion; four-leg; four-wire; pulse width modulation; optimization; switching losses; grid-connected

1. Introduction

The capability to handle neutral current is gaining interest in grid-connected power applications such as distributed generation systems [1,2], active rectifiers [3,4], and power filters [5]. Particular attention to this feature has been drawn by developing a new generation of electric vehicle (EV) charging infrastructures that are moving towards smart services known as vehicle-to-grid (V2G) and vehicle-for-grid (V4G), where four wire front-end solutions are widely adopted [6]. Among the multiple topologies available in the literature/market, three topologies are commonly utilized: split-capacitor [7,8], four-leg [6,9], and independently controlled neutral module [10]. These voltage source inverters (VSIs) can either have or do not have a neutral inductor in the fourth wire.

The two main pulse width modulation (PWM) techniques are space vector pulse width modulation (SVPWM) and carrier-based pulse width modulation (CBPWM). Although SVPWM guarantees a more straightforward understanding of the modulation theory, it has been outcompeted by the implementation simplicity of CBPWM in both analog and digital systems [11,12]. One of their main differences is the way they employ their degrees of freedom. In space vector modulation (SVM), it corresponds to the criterion used for sharing two 'zero' states. On the other hand, in the carrier-

based (CB) implementation, it corresponds to the additive common-mode injection into the modulating signals. It has been demonstrated that SVPWM leads to the identical CBPWM gate signals pattern, and therefore, their performances are coinciding [13]. In the current paper, CB methodology has been employed, although the same results could have been obtained with the SVM approach as well.

The two first-discovered CB modulation schemes are sinusoidal pulse width modulation (SPWM) and centered pulse width modulation (CPWM). Over the last decades, discontinuous pulse width modulation (DPWM) was introduced to reduce the number of commutations, consequently, increase the efficiency of high-power converters [14]. This objective is obtained by clamping for one-third of the fundamental period each phase modulating signal to either the positive (DPWMMAX) or the negative (DPWMMIN) linear limits, avoiding any intersection with the carrier signal. In this class of injections (DPWM), the average switching frequency is equal to two-thirds of the one experienced in SPWM and CPWM. Soon after, new discontinuous injections were introduced, namely DPWM0, DPWM1, DPWM2, and DPWM3 [12,15–17]. In general, by alternating positive and negative clamping across a fundamental cycle, one could obtain virtually infinite discontinuous injections. With the specific task to reduce the switching losses in accordance with the required power factor, generalized discontinuous pulse width modulation (GDPWM) has been proposed. In the best working area, it is capable of halving losses associated with switches' commutations [18–20].

However, the modulation principle does affect not only the switching losses but also the current ripple visible on the ac side of the converter. It is recognized that the current ripple has primary importance when it comes to satisfying grid compliance standards, filter design, efficiency evaluation, and optimization of modulation techniques. Furthermore, the current ripple analysis is critical for compensating inverter nonlinearities [21]. It could be used for designing active filter control systems and hysteresis current controllers [22]. Finally, variable switching frequency strategy can be developed basing on the knowledge of the ripple distribution over a fundamental period [23].

With reference to three-phase, three-wire inverter structure, a wide variety of publications is already available. In particular, the ripple peak-to-peak as a function of modulation index has been provided in [24]. Moreover, [25] compares ac current ripple characteristics in two-level and multilevel converts. The comparison of ac current ripple in DPWM and CPWM is given in [26], permitting optimization of inverter operation by amending the average switching frequency.

Concerning the four-leg three-phase VSI configurations, only a few contributions have addressed the current ripple topic. In [6], the maximum peak-to-peak current ripple has been compared with the three-wire counterpart without providing any ripple profile in the fundamental cycle or rms estimation in either phase or neutral current. Although [27] proposed an envelope and rms evaluation, it has been done for SPWM injection only. Many authors have optimized specific inverter parameters in the four-leg topology. In particular, common-mode voltage and current are reduced by employing multiple carriers in [28]. Power loss reduction at high values of modulating index is achieved in [29] through dedicated common-mode injections. Finally, a neutral inductor designing procedure for SPWM-based inverters has been proposed in [30].

To the best of the authors' knowledge, no manuscript has provided an extensive analytical ac current ripple evaluation of the peak-to-peak, envelopes, and rms, for both phase and neutral current with common-mode injections different from SPWM. Prior to this study, neither average switching frequency nor switching losses, in the case of DPWM, have not been taken into account to optimize the performance of four-leg inverters. The target of this manuscript is to provide a thorough analytical description of the phase and neutral current ripple characteristics in three-phase, two-level, four-leg, grid-connected inverters for the most popular PWM schemes, such as SPWM, CPWM, DPWM, and third harmonic injection (THIPWM). Current ripple envelopes (peak values) have been determined in the whole fundamental period, and true rms expressions have been derived as a function of modulation index. Focusing solely on grid-connected applications, 'balanced' grid voltages have been considered in the current ripple analysis for both phase and neutral findings. Due to small ac coupling reactance (usually 0.05–0.08 p.u.), relevant unbalanced currents can be driven by slightly asymmetric inverter voltages. Therefore, the three modulating signals can be considered

quasi-balanced leading to a unique modulation index. The aim of this assumption is to simplify computation efforts while preserving the applicability of the derived expressions in grid-connected applications.

Another contribution given by this work is a comparison of the considered modulation strategies in terms of different metrics, i.e., switching losses, average switching frequency, rms and peak-to-peak of ac current ripple. Specifically, the comparison is realized equalizing one of the metric parameters and comparing the others. This procedure allows indicating which PWM injection could most effectively match optimization problems during the inverter design procedure. All the analytical expressions have been broadly verified by performing numerical simulations and laboratory experiments for each of the considered modulation case. The excellent matching ensures the validity and accuracy of the analytical evaluations.

The paper is organized as follows. Section 2 provides basic assumptions on the considered topology and the carrier-based common-mode injection. In Section 3, a review of the DPWM injection classes is provided. Then, ripple performance examinations for phase currents and neutral current are presented in Section 4 and 5, respectively. Experimental results that are exhibited to validate the provided ripple study are given in Section 6. Finally, conclusions are drawn, summarizing the key outcomes of this paper.

2. Basic Assumptions and Carrier-Based Modulation Principle

2.1. Converter Model and Current Ripple Definition

The converter configuration consists of four identical legs, each of them made up of two switches (as shown in Figure 1). The four-leg VSI is supplied by a constant dc source (V_{dc}) and tied up with the grid through magnetically independent ac-link inductors (L). The middle point (n) of the fourth leg is directly linked with the neutral point of a load/grid. Another popular three-phase, four-wire VSI configuration, namely four-leg VSI with the four-inductor arrangement (an inductor placed in each phase and neutral), is outside the scope of this paper. It has already been mentioned that this paper has the aim to report ac current ripple analysis in grid-tied applications, leading to an examination of unity power factor circuits. Nevertheless, for the sake of clarity, it must be mentioned that the ac current ripple characteristics are independent of the phase angle φ, so all of the expressions presented below are equally valid for any abstract power factor.

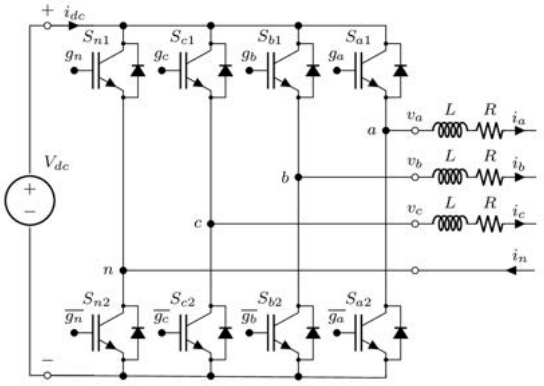

Figure 1. Circuit scheme of a three-phase four-leg inverter.

Concerning the considered system, the three-phase reference voltages are given by:

$$\begin{cases} \bar{v}_a(\vartheta) = m_a\, V_{dc} \cos(\vartheta) \\ \bar{v}_b(\vartheta) = m_b\, V_{dc} \cos\left(\vartheta - \dfrac{2\pi}{3}\right) \\ \bar{v}_c(\vartheta) = m_c\, V_{dc} \cos\left(\vartheta + \dfrac{2\pi}{3}\right) \end{cases} \quad (1)$$

where m_a, m_b, and m_c represent modulation indices of phase voltages $\bar{v}_a$, $\bar{v}_b$, and $\bar{v}_c$, respectively; $\vartheta = \omega t$ is the phase angle, and ω is the fundamental (grid) angular frequency. The modulation index here is defined as the ratio between the amplitude of phase voltage fundamental component and dc bus voltage, so the signal modulation range, in per unit, is ±0.5 [27]. In the case of balanced modulation, $m_a = m_b = m_c = m$, so the subscripts are omitted. Likewise, in some cases, the common-mode injections are independent from cross-referencing phase modulating signals. Therefore, the related findings are expressed with subscript x, which can be freely replaced with the considered phase (a, b, and c). This general notation also implies its validity independently from the case study, balanced or unbalanced. At the same time, in cumbersome computations, the balanced conditions have been assumed only, and, therefore, no subscript has been introduced (assuming generally balanced modulation index m).

Furthermore, it must be highlighted that in most of the grid-connected applications, it is natural to drive unbalanced currents by means of even small modulation index unbalances (in the order of a few percent). Therefore, it is acceptable to assume having unbalanced currents at $m_a \cong m_b \cong m_c = m$. As will be shown further, this presumption does not introduce detrimental effects on the validity of the findings. From now on, the notation i_x and i_n refers to phase and neutral currents, respectively.

The current ripple can be seen as an integral of the instantaneous voltage difference between the output voltage and the sinusoidal reference voltage in (1). This expression, neglecting the voltage drop on the resistance (R), can be written as:

$$\hat{\imath}_x(t) \cong \hat{\imath}_x(0) + \frac{1}{L}\int_0^t [v_x(t) - \bar{v}_x(t)]dt \tag{2}$$

where $\hat{\imath}_x$ is the switching current ripple component and v_x is the instantaneous voltage.

The amplitude of the peak-to-peak current ripple over a switching period T_{sw} can be defined as:

$$\hat{\imath}_{pp}(t) = \max[\hat{\imath}_x(t)]|_{T_{sw}} - \min[\hat{\imath}_x(t)]|_{T_{sw}} \tag{3}$$

The inverter instantaneous voltage v_x is expressed as:

$$v_x(t) = V_{dc}\big(g_x(t) - g_n(t)\big) \tag{4}$$

corresponding to the difference between the phase and the neutral pole voltages defined by the mean of their respective gate signals g_x and g_n.

2.2. Carrier-Based Common-Mode Injection

In the carrier-based implementation, it is possible to achieve multiple optimizations for a considered modulation method, some of them are higher dc-link utilization (maximization of the modulation index) and reduction of commutations in each fundamental period. This procedure consists of injecting into all sine-like modulating signals the common-mode component $\gamma(\vartheta)$, as:

$$\begin{gathered} u_a^*(\vartheta) = u_a(\vartheta) + \gamma(\vartheta) \\ u_b^*(\vartheta) = u_b(\vartheta) + \gamma(\vartheta) \\ u_c^*(\vartheta) = u_c(\vartheta) + \gamma(\vartheta) \\ u_n(\vartheta) = \gamma(\vartheta) \end{gathered} \tag{5}$$

where u_x is the reference phase voltage of (1) scaled by a factor of V_{dc} and u_n is the neutral leg modulating signal.

In SPWM, the common-mode component is kept equal to zero in the whole fundamental cycle. Despite the simplicity of the implementation, it does not provide any benefits neither in dc-bus voltage utilization (the modulation index m_x is ranging from 0 up to 0.5) nor in minimization of switching losses. Equation (6) shows the SPWM common-mode injection.

$$\gamma(\vartheta)|_{\mathrm{SPWM}} = 0 \tag{6}$$

On the other hand, it is feasible to maximize the dc-link voltage utilization by means of the so-called centered PWM (CPWM). It can be considered as the carrier-based implementation of the space vector PWM (SVPWM), and it shares the same benefits of a +15% bus utilization improvement (modulation index can reach $1/\sqrt{3}$). Its mathematical definition can be derived from the following magnitude test:

$$\gamma(\vartheta)|_{\mathrm{CPWM}} = -\frac{1}{2}\{\max[u_a(\vartheta), u_b(\vartheta), u_c(\vartheta)] + \min[u_a(\vartheta), u_b(\vartheta), u_c(\vartheta)]\} \quad (7)$$

However, CPWM is not the only one modulation strategy that can maximize the dc-link utilization. In this context, DPWM methods can be useful as well. One could identify a set of modulation schemes that can provide a lower amount of commutations in one fundamental period diminishing switching losses. In Section 3, the most common DPWM injections are explained in detail.

For the sake of completeness, THIPWM is discussed here as well. Due to the rigorous procedure that is necessary for generating a third harmonic signal, this class of injection has lost its industrial and academic interest. The two most popular injections of this kind are THIPWM1/6 and THIPWM1/4, which respectively have a magnitude of one-sixth and one-quarter of the fundamental component. They can be analytically described as:

$$\gamma(\vartheta)|_{\mathrm{THIPWM1/6}} = -\frac{m}{6}\cos(3\vartheta) \quad (8)$$

$$\gamma(\vartheta)|_{\mathrm{THIPWM1/4}} = -\frac{m}{4}\cos(3\vartheta) \quad (9)$$

Differently from SPWM, CPWM, and some of the DPWM injections, THIPWM, with definitions given in Equations (8) and (9), can be effectively employed on a balanced system only [12]. Moreover, THIPWM1/4 reaches only +12% in bus utilization in comparison with CPWM. Due to the mentioned drawbacks, THIPWM has been commonly replaced with more practical CPWM/SVPWM injections. All the here discussed injections are depicted in Figure 2 at m = 0.5.

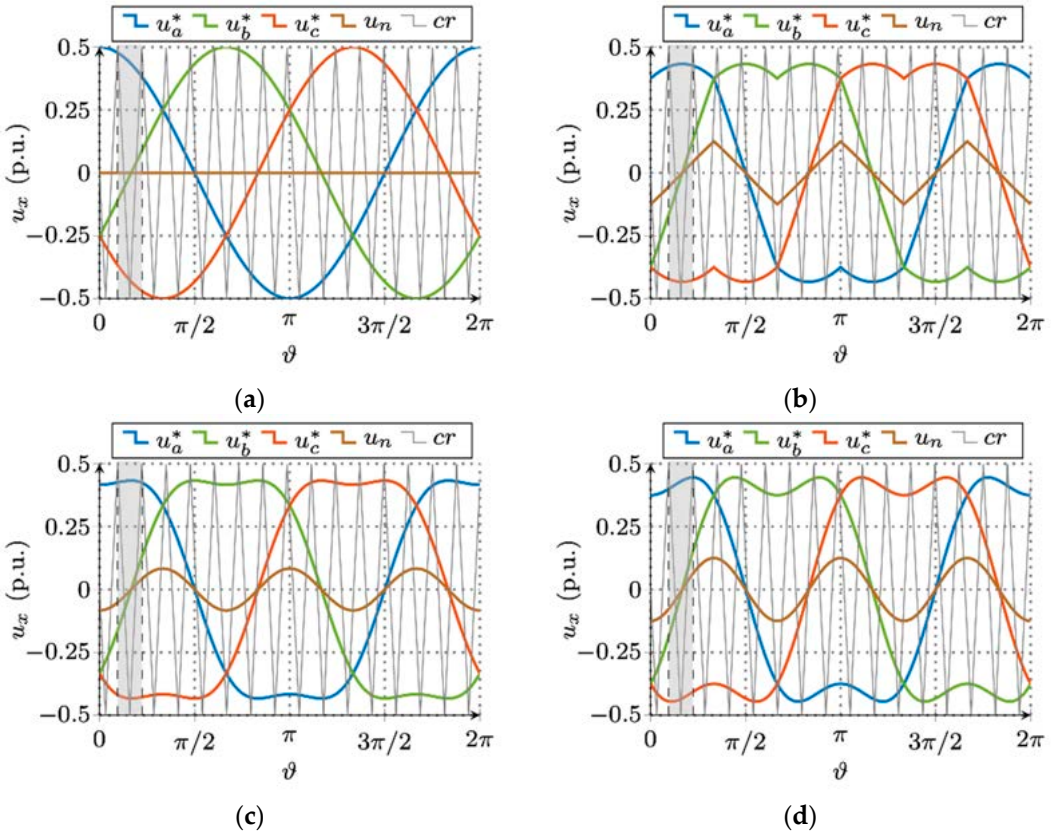

Figure 2. Phase (u^*) and neutral (u_n) modulating signals (at m = 0.5) of: (**a**) SPWM; (**b**) CPWM; (**c**) THIPWM1/6; and (**d**) THIPWM1/4.

3. Discontinuous PWM Review

Similarly to CPWM/SVPWM, DPWM enlarges the voltage utilization range up to $m = 1/\sqrt{3}$. However, the main feature of this modulation class is in switching losses reduction. All the DPWM injections here studied, decrease by one third in the number of switching operations in each

fundamental cycle. This feature is achieved by the injection of a proper common-mode signal $\gamma(\vartheta)$, which can "shift" the modulating signals in a position that guarantees, at any switching instance, at least one non-commutating leg.

3.1. DPWMMAX and DPWMMIN

The two most popular DPWM injections are DPWMMAX and DPWMIN, in the following equations and figures labeled as DMAX and DMIN, respectively. They consistently clamp one of the modulating signals to the maximum (0.5) or minimum (−0.5) value, respectively. The common-mode injection can be obtained through:

$$\gamma(t)|_{\mathrm{DMAX}} = \frac{1}{2} - \max[u_a(\vartheta), u_b(\vartheta), u_c(\vartheta)] \tag{10}$$

$$\gamma(t)|_{\mathrm{DMIN}} = -\frac{1}{2} - \min[u_a(\vartheta), u_b(\vartheta), u_c(\vartheta)] \tag{11}$$

By assuming a balanced system (unique modulation index for all phases), Equations (10) and (11) can be explicitly rewritten as:

$$\gamma(\vartheta)|_{\mathrm{DMAX}} = \frac{1}{2} - \begin{cases} m\cos\left(\vartheta + \frac{2\pi}{3}\right) & -\pi \le \vartheta \le -\frac{\pi}{3} \\ m\cos(\vartheta) & -\frac{\pi}{3} \le \vartheta \le \frac{\pi}{3} \\ m\cos\left(\vartheta - \frac{2\pi}{3}\right) & \frac{\pi}{3} \le \vartheta \le \pi \end{cases} \tag{12}$$

$$\gamma(\vartheta)|_{\mathrm{DMIN}} = -\frac{1}{2} - \begin{cases} m\cos\left(\vartheta + \frac{2\pi}{3}\right) & 0 \le \vartheta \le \frac{2\pi}{3} \\ m\cos(\vartheta) & \frac{2\pi}{3} \le \vartheta \le \frac{4\pi}{3} \\ m\cos\left(\vartheta - \frac{2\pi}{3}\right) & \frac{4\pi}{3} \le \vartheta \le 2\pi \end{cases} \tag{13}$$

Both DPWMMAX and DPWMMIN are depicted in Figure 3. It is visible that, for one-third of the fundamental period, modulating signals u^* do not intersect the carrier cr and therefore do not cause commutations.

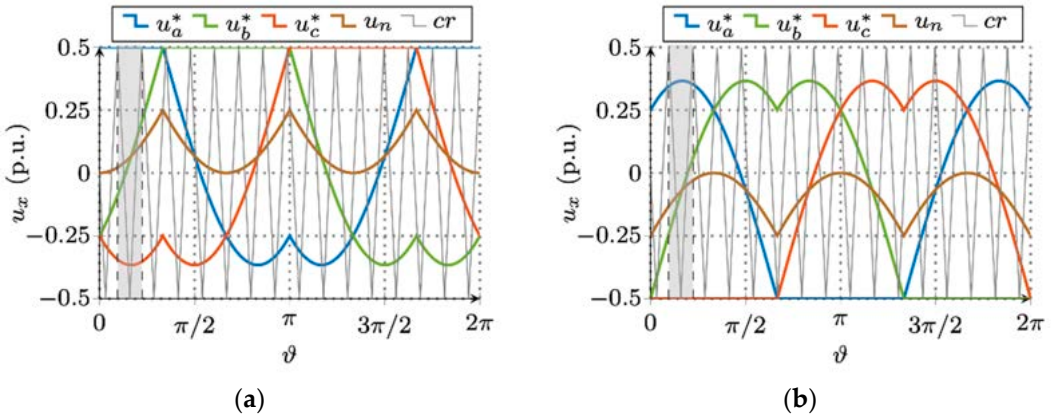

Figure 3. Phase (u^*) and neutral (u_n) modulating signals for: (**a**) DPWMMAX; and (**b**) DPWMMIN.

It can be easily noticed that:

$$\gamma(\vartheta)|_{\mathrm{DMAX}} = -\gamma(\vartheta + \pi)|_{\mathrm{DMIN}} \tag{14}$$

Moreover, since both Equations (12) and (13) are unipolar, one could claim that both injections do not share the advantage of the half-wave symmetry properties. Therefore, the modulating signals are not half-wave symmetric as well. This last statement suggests already that the current ripple waveform must be studied on the whole fundamental period rather than only on half-cycle (as

typically done in most of the injections). However, by examining Equation (14), it is possible to state that (for phase *a)*:

$$u_a^*(\vartheta)|_{\mathrm{DMAX}} = u_a(\vartheta) + \gamma(\vartheta)|_{\mathrm{DMAX}} = \begin{cases} u_a(\vartheta) + \gamma(\vartheta)|_{\mathrm{DMAX}} & -\frac{\pi}{2} \le \vartheta \le \frac{\pi}{2} \\ -[u_a(\vartheta - \pi) + \gamma(\vartheta - \pi)|_{\mathrm{DMIN}}] & \frac{\pi}{2} \le \vartheta \le \frac{3\pi}{2} \end{cases} \tag{15}$$

$$u_a^*(\vartheta)|_{\mathrm{DMIN}} = u_a(\vartheta) + \gamma(\vartheta)|_{\mathrm{DMIN}} = \begin{cases} u_a(\vartheta) + \gamma(\vartheta)|_{\mathrm{DMIN}} & -\frac{\pi}{2} \le \vartheta \le \frac{\pi}{2} \\ -[u_a(\vartheta - \pi) + \gamma(\vartheta - \pi)|_{\mathrm{DMAX}}] & \frac{\pi}{2} \le \vartheta \le \frac{3\pi}{2} \end{cases} \tag{16}$$

Thanks to Equation (15), one can study the second half cycle of the current ripple, in case of DPWMMAX, referring to the opposite of the first half cycle in the case of DPWMMIN. Similarly, with Equation (16), one could examine ripple in the case of DPWMMIN taking advantage of DPWMMAX computations. This relationship between the two injections suggests that their performance in terms of current ripple peak-to-peak and rms is the same.

In general, this statement can be extended by saying that:

$$u_x^*(\vartheta)|_{\mathrm{DMAX}} = -u_x^*(\vartheta + \pi)|_{\mathrm{DMIN}} \tag{17}$$

3.2. Generalized DPWM

By alternating both DPWMMAX and DPWMMIN, there is a possibility to obtain virtually an infinite number of DPWM injections. In this context, one could find, in the literature, the so-called generalized DPWM (GDPWM).

From the analytical point of view, it is necessary to introduce a set of dummy signals u_s that could be defined by shifting their angle as:

$$u_s(\vartheta, \psi_m) = u(\vartheta + \psi_m) \tag{18}$$

where ψ_m is a phase angle that can range in the interval of $[-\pi/6; \pi/6]$.

GDPWM injection can be obtained throughout the magnitude test Equation (19), as in [12].

$$\gamma(\vartheta, \psi_m)|_{\mathrm{GDPWM}} = \begin{cases} \frac{1}{2}\mathrm{sign}[u_a(\vartheta)] - u_a(\vartheta) & |u_a(\vartheta, \psi_m)|_s| \ge |u_b(\vartheta, \psi_m)|_s|, |u_c(\vartheta, \psi_m)|_s| \\ \frac{1}{2}\mathrm{sign}[u_b(\vartheta)] - u_b(\vartheta) & |u_b(\vartheta, \psi_m)|_s| \ge |u_a(\vartheta, \psi_m)|_s|, |u_c(\vartheta, \psi_m)|_s| \\ \frac{1}{2}\mathrm{sign}[u_c(\vartheta)] - u_c(\vartheta) & |u_c(\vartheta, \psi_m)|_s| \ge |u_a(\vartheta, \psi_m)|_s|, |u_b(\vartheta, \psi_m)|_s| \end{cases} \tag{19}$$

The three most common injections of this kind are DPWM0, DPWM1, and DPWM2.

3.2.1. DPWM0

By replacing $\psi_m = -\pi/6$ into Equations (18) and (19), it yields to:

$$\gamma(\vartheta)|_{\mathrm{DPWM0}} = \begin{cases} \gamma(\vartheta)|_{\mathrm{DMAX}} & -\pi \le \vartheta \le -\frac{2\pi}{3} \quad -\frac{\pi}{3} \le \vartheta \le 0 \quad \frac{\pi}{3} \le \vartheta \le \frac{2\pi}{3} \\ \gamma(\vartheta)|_{\mathrm{DMIN}} & -\frac{2\pi}{3} \le \vartheta \le -\frac{\pi}{3} \quad 0 \le \vartheta \le \frac{\pi}{3} \quad \frac{2\pi}{3} \le \vartheta \le \pi \end{cases} \tag{20}$$

3.2.2. DPWM1

By substituting $\psi_m = 0$ into Equations (18) and (19), one could obtain:

$$\gamma(\vartheta)|_{\mathrm{DPWM1}} = \begin{cases} \gamma(\vartheta)|_{\mathrm{DMAX}} & -\frac{5\pi}{6} \le \vartheta \le -\frac{\pi}{2} \quad -\frac{\pi}{6} \le \vartheta \le \frac{\pi}{6} \quad \frac{\pi}{2} \le \vartheta \le \frac{5\pi}{6} \\ \gamma(\vartheta)|_{\mathrm{DMIN}} & -\frac{\pi}{2} \le \vartheta \le -\frac{\pi}{6} \quad \frac{\pi}{6} \le \vartheta \le \frac{\pi}{2} \quad \frac{5\pi}{6} \le \vartheta \le \frac{7\pi}{6} \end{cases} \tag{21}$$

3.2.3. DPWM2

By introducing $\psi_m = \pi/6$ into Equations (18) and (19), the common-mode injection takes the form:

$$\gamma(\vartheta)|_{\mathrm{DPWM2}} = \begin{cases} \gamma(\vartheta)|_{\mathrm{DMIN}} & -\pi \le \vartheta \le -\frac{2\pi}{3} \quad -\frac{\pi}{3} \le \vartheta \le 0 \quad \frac{\pi}{3} \le \vartheta \le \frac{2\pi}{3} \\ \gamma(\vartheta)|_{\mathrm{DMAX}} & -\frac{2\pi}{3} \le \vartheta \le -\frac{\pi}{3} \quad 0 \le \vartheta \le \frac{\pi}{3} \quad \frac{2\pi}{3} \le \vartheta \le \pi \end{cases} \tag{22}$$

3.3. DPWM3

Another popular injection is the so-called DPWM3. Likewise, DPWMMAX, DPWMMIN, and GDPWM, it is based on the magnitude test. However, this time the leading signal is the one that has intermediate magnitude [12]:

$$\gamma(\vartheta)|_{\mathrm{DPWM3}} = \begin{cases} \frac{1}{2}\mathrm{sign}[u_a(\vartheta)] - u_a(\vartheta) & \begin{cases} |u_b(\vartheta)| \ge |u_a(\vartheta)| \ge |u_c(\vartheta)| \\ |u_c(\vartheta)| \ge |u_a(\vartheta)| \ge |u_b(\vartheta)| \end{cases} \\ \frac{1}{2}\mathrm{sign}[u_b(\vartheta)] - u_b(\vartheta) & \begin{cases} |u_a(\vartheta)| \ge |u_b(\vartheta)| \ge |u_c(\vartheta)| \\ |u_c(\vartheta)| \ge |u_b(\vartheta)| \ge |u_a(\vartheta)| \end{cases} \\ \frac{1}{2}\mathrm{sign}[u_c(\vartheta)] - u_c(\vartheta) & \begin{cases} |u_a(\vartheta)| \ge |u_c(\vartheta)| \ge |u_b(\vartheta)| \\ |u_b(\vartheta)| \ge |u_c(\vartheta)| \ge |u_a(\vartheta)| \end{cases} \end{cases} \tag{23}$$

In the same manner, this injection can be seen as an alternation of DPWMMAX and DPWMMIN:

$$\gamma(\vartheta)|_{\mathrm{DPWM3}} = \begin{cases} \gamma(\vartheta)|_{\mathrm{DMIN}} & -\frac{5\pi}{6} \le \vartheta \le -\frac{\pi}{2} \quad -\frac{\pi}{6} \le \vartheta \le \frac{\pi}{6} \quad \frac{\pi}{2} \le \vartheta \le \frac{5\pi}{6} \\ \gamma(\vartheta)|_{\mathrm{DMAX}} & -\frac{\pi}{2} \le \vartheta \le -\frac{\pi}{6} \quad \frac{\pi}{6} \le \vartheta \le \frac{\pi}{2} \quad \frac{5\pi}{6} \le \vartheta \le \frac{7\pi}{6} \end{cases} \tag{24}$$

Here one crucial notice must be made that differently from DPWMMAX and DPWMMIN, it is not possible to use GDPWM and DPWM3 in case of unbalanced modulation, having $m_x \neq m$.

From Figure 4, one can note that DPWM0, DPWM1, DPWM2, and DPWM3 alternate every 60° the injections introduced by DPWMMAX and DPWMMIN. Moreover, the injection $\gamma(\vartheta)$, in these four cases, is half-wave symmetric. Thus, the modulating signals and the related current ripple are half-wave symmetric as well. As a result, the ripple analysis can be limited to one half fundamental cycle.

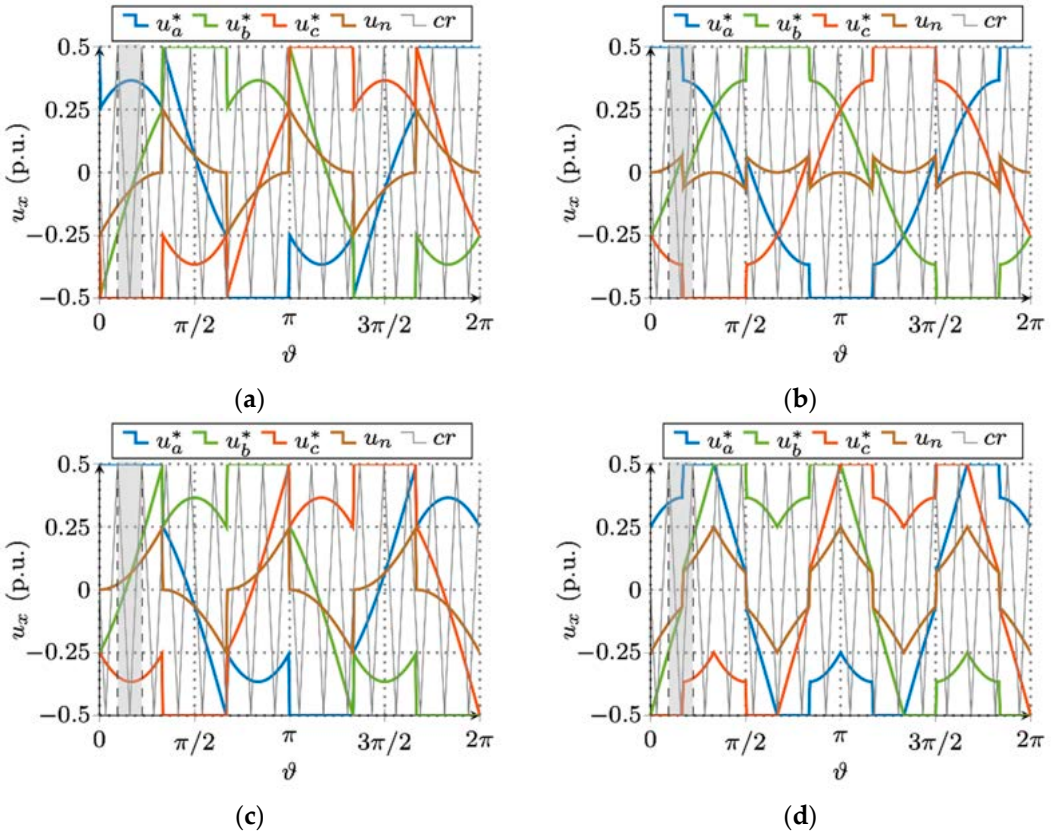

Figure 4. Phase (u^*) and neutral (u_n) modulating signals for: (**a**) DPWM0; (**b**) DPWM1; (**c**) DPWM2; and (**d**) DPWM3.

Because of Equation (17), it can be observed that DPWM0 and DPWM2 have the same ripple performance as DPWMMAX and DPWMMIN in terms of maximum peak-to-peak and rms values.

4. Phase Currents Ripple Analysis

By considering one switching period of a generic injection, the ac current ripple and the voltage pulse disposition could be depicted as in Figure 5. The pulse arrangement employed in this section should be considered valid only for $u \geq 0$, namely in case of phase a from $-\pi/2$ to $\pi/2$. As already thoroughly discussed in the previous sections, due to symmetry reasons, it is possible to restrict the analysis to half of a fundamental period by adopting the assumption above. All the findings shown in this section can be extended to the other phases.

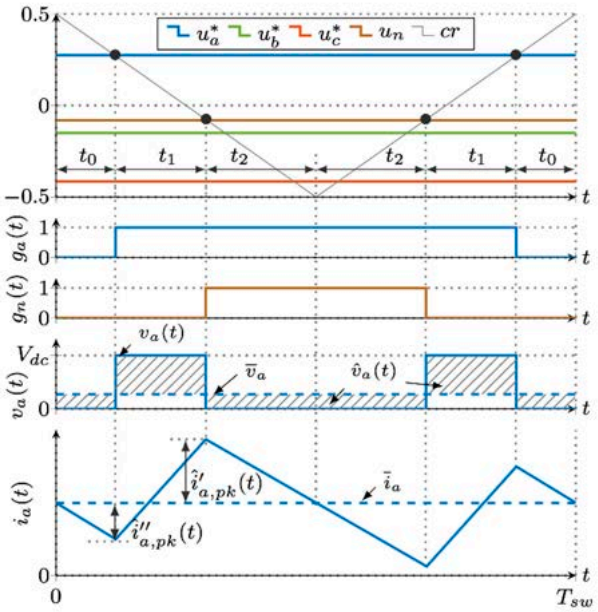

Figure 5. Current ripple waveform (phase *a*) (bottom) and voltage pulse disposition (phase *a*) (middle) generated by a generic modulation strategy in one switching period (top).

Regarding Figure 5, the pulse timing about phase *a* could be identified as:

$$\begin{cases} t_0 = \dfrac{T_{sw}}{2}\left(\dfrac{1}{2} - u_a^*(t)\right) = \dfrac{T_{sw}}{2}\left(\dfrac{1}{2} - u_a(t) - \gamma(t)\right) \\ t_1 = \dfrac{T_{sw}}{2}\left(u_a^*(t) - u_n(t)\right) = \dfrac{T_{sw}}{2}u_a(t) \qquad\qquad u_a(t) \geq 0 \\ t_2 = \dfrac{T_{sw}}{2}\left(\dfrac{1}{2} + u_n(t)\right) = \dfrac{T_{sw}}{2}\left(\dfrac{1}{2} + \gamma(t)\right) \end{cases} \tag{25}$$

Moreover, with (26) two local maxima, indicated as primary and secondary, can be defined.

$$\begin{cases} \hat{\imath}'_{a,pk}(t) = t_2\dfrac{V_{dc}}{L}u_a(t) = \dfrac{V_{dc}}{2Lf_{sw}}u_a(t)\left[\dfrac{1}{2} + \gamma(t)\right] \\ \hat{\imath}''_{a,pk}(t) = -t_0\dfrac{V_{dc}}{L}u_a(t) = \dfrac{V_{dc}}{2Lf_{sw}}u_a(t)\left[-\dfrac{1}{2} + u_a(t) + \gamma(t)\right] \end{cases} \quad u_a(t) \geq 0 \tag{26}$$

Equation (26) is the base of the following analysis of current ripple peak-to-peak and rms values, and it is valid regardless of the kind of injection $\gamma(t)$ has been considered. It must be emphasized here that the total current ripple is composed by primary and secondary peaks, where the latter ones are usually omitted by researchers, despite playing significant role in true rms computation, as it will be shown in Section 4.2.

4.1. Phase Current Ripple Profile

By extending Equation (26) to the whole fundamental period [0; 2π], one could find the actual current ripple envelopes that enclose primary and secondary peaks. It can be demonstrated that when $u \leq 0$, primary and secondary envelopes can be mathematically described as:

$$\begin{cases} \hat{\imath}'_{a,pk}(t) = -\left(\frac{T_{sw}}{2} - t_2\right)\frac{V_{dc}}{L}u_a(t) = \frac{V_{dc}}{2Lf_{sw}}u_a(t)\left[-\frac{1}{2} + \gamma(t)\right] \\ \hat{\imath}''_{a,pk}(t) = \left(\frac{T_{sw}}{2} - t_0\right)\frac{V_{dc}}{L}u_a(t) = \frac{V_{dc}}{2Lf_{sw}}u_a(t)\left[\frac{1}{2} + u_a(t) + \gamma(t)\right] \end{cases} \quad u_a(t) \leq 0 \tag{27}$$

Therefore, by combining Equations (26) and (27), the envelope expressions (positive and negative) are valid in the whole fundamental period and could be written as:

$$\begin{cases} \hat{\imath}'_{a,pk}(t) = \pm\frac{V_{dc}}{2Lf_{sw}}u_a(t)\left\{\frac{1}{2}\text{sign}[u_a(t)] + \gamma(t)\right\} \\ \hat{\imath}''_{a,pk}(t) = \pm\frac{V_{dc}}{2Lf_{sw}}u_a(t)\left\{-\frac{1}{2}\text{sign}[u_a(t)] + u_a(t) + \gamma(t)\right\} \end{cases} \tag{28}$$

Equation (28) can be normalized (using as a base $V_{dc}/(2Lf_{sw})$) yielding:

$$\begin{cases} \hat{r}'_{a,pk}(t) = \pm u_a(t)\left\{\frac{1}{2}\text{sign}[u_a(t)] + \gamma(t)\right\} \\ \hat{r}''_{a,pk}(t) = \pm u_a(t)\left\{-\frac{1}{2}\text{sign}[u_a(t)] + u_a(t) + \gamma(t)\right\} \end{cases} \tag{29}$$

The same normalization factor has been adopted to normalize the phase currents. Equations (28) and (29) are also valid in unbalanced conditions, i.e., modulation indices different (only in linear modulation range).

For verifying the accuracy of Equation (29), simulation results for examined injections are presented from Figures 6–15. Subfigures marked with "(a)" demonstrate the actual capability of the topology to carry unbalanced currents in all the presented injections. The normalized current ripple component of phase *a* has been presented in subfigures labeled as "(b)". A relatively low switching frequency (f_{sw} = 3.6 kHz) has been chosen to clearly show the ripple profile with its primary and secondary envelopes.

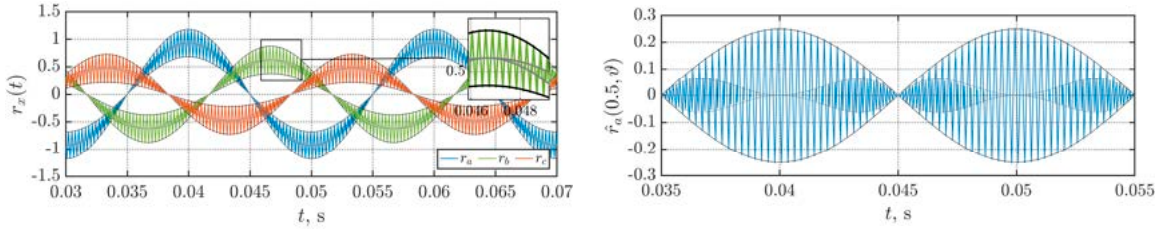

(**a**) (**b**)

Figure 6. Primary (black) and secondary (gray) envelopes in case of SPWM at m = 0.5 and f_{sw} = 3.6 kHz: (**a**) Normalized phase currents; (**b**) Normalized phase current ripple.

It is noteworthy that CPWM (Figure 7), THIPWM1/6 (Figure 8), and THIPWM1/4 (Figure 9), share a similar profile of the common-mode signal (third harmonic of the fundamental component is dominant), their ripple contours are visually similar. Therefore, their performance in terms of peak-to-peak and rms is expected to be close to one another.

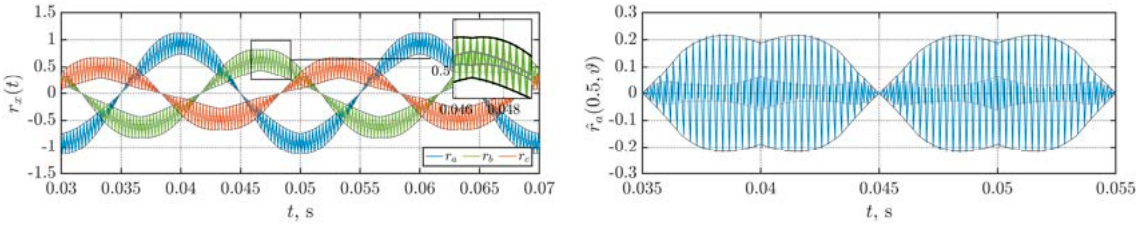

(**a**) (**b**)

Figure 7. Primary (black) and secondary (gray) envelopes in case of CPWM at m = 0.5 and f_{sw} = 3.6 kHz: (**a**) Normalized phase currents; (**b**) Normalized phase current ripple.

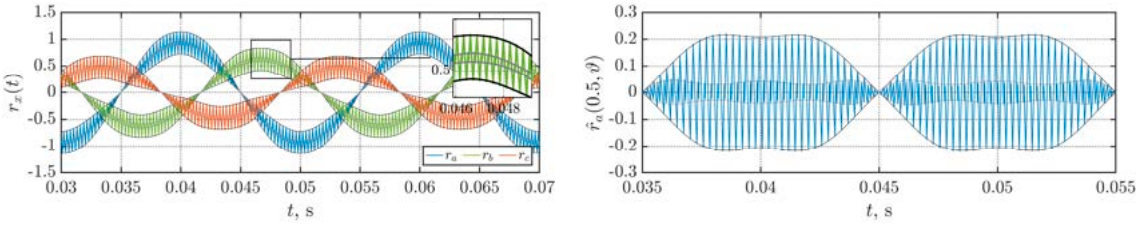

(**a**) (**b**)

Figure 8. Primary (black) and secondary (gray) envelopes in case of THIPWM1/6 at m = 0.5 and f_{sw} = 3.6 kHz: (**a**) Normalized phase currents; (**b**) Normalized phase current ripple.

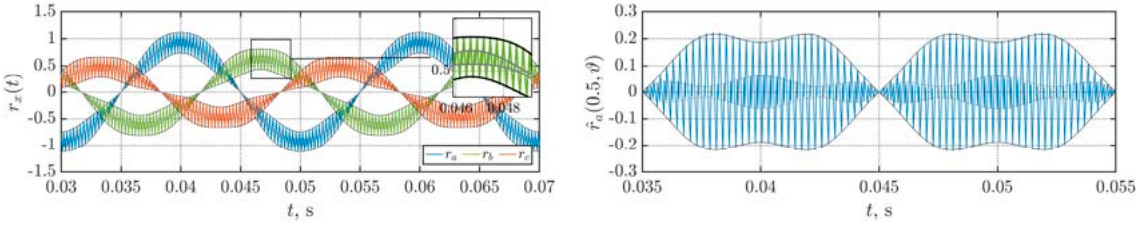

(**a**) (**b**)

Figure 9. Primary (black) and secondary (gray) envelopes in case of THIPWM1/4 at m = 0.5 and f_{sw} = 3.6 kHz: (**a**) Normalized phase currents; (**b**) Normalized phase current ripple.

As discussed before, DPWMMAX (Figure 10) and DPWMMIN (Figure 11) do not present a half-wave symmetry. However, as it has been shown in (17) for their modulating signals, also the current ripple could be interchangeably examined by DPWMMAX or DPWMMIN, but half-cycle displaced (+π). Both envelopes match with the simulation profiles.

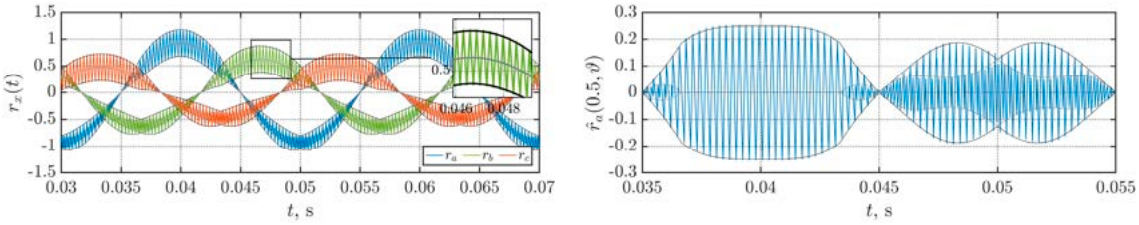

(**a**) (**b**)

Figure 10. Primary (black) and secondary (gray) envelopes in case of DPWMMAX at m = 0.5 and f_{sw} = 3.6 kHz: (**a**) Normalized phase currents; (**b**) Normalized phase current ripple.

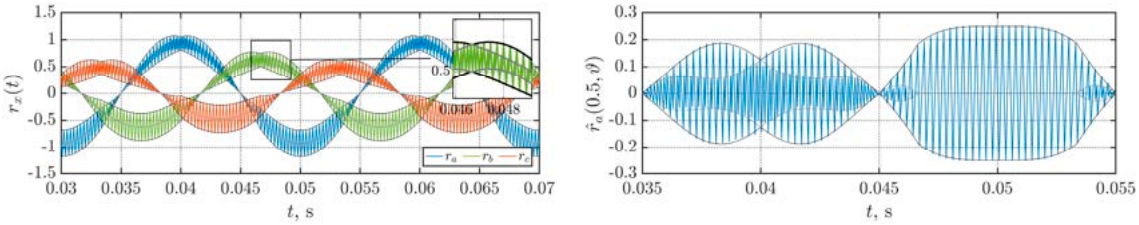

(**a**) (**b**)

Figure 11. Primary (black) and secondary (gray) envelopes in case of DPWMMIN at m = 0.5 and f_{sw} = 3.6 kHz: (**a**) Normalized phase currents; (**b**) Normalized phase current ripple.

Since DPWM0 (Figure 12), DPWM1 (Figure 13), DPWM2 (Figure 14), and DPWM3 (Figure 15) alternate the positive and the negative clamping, their ripple profiles share part of the DPWMMAX and DPWMMIN contours. Moreover, rearranging sections of the plots in Figures 12b and 14b, it is possible to obtain the profiles given in Figures 10b and 11b, ensuring the same ripple characteristics of DPWMMAX and DPWMMIN. Again, in all the cases, analytical envelopes correctly bound numerically obtained current patterns.

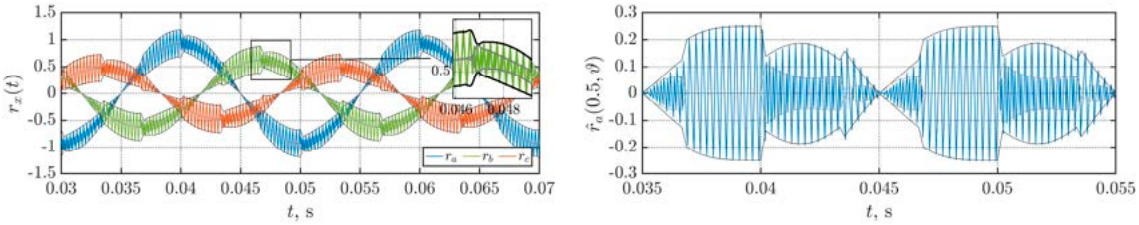

(**a**) (**b**)

Figure 12. Primary (black) and secondary (gray) envelopes in case of DPWM0 at m = 0.5 and f_{sw} = 3.6 kHz: (**a**) Normalized phase currents; (**b**) Normalized phase current ripple.

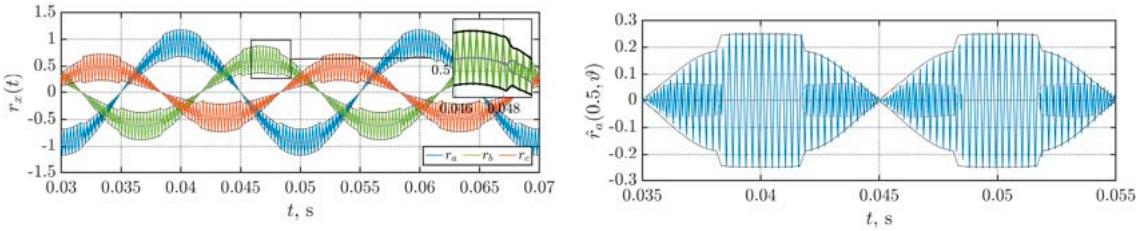

(**a**) (**b**)

Figure 13. Primary (black) and secondary (gray) envelopes in case of DPWM1 at m = 0.5 and f_{sw} = 3.6 kHz: (**a**) Normalized phase currents; (**b**) Normalized phase current ripple.

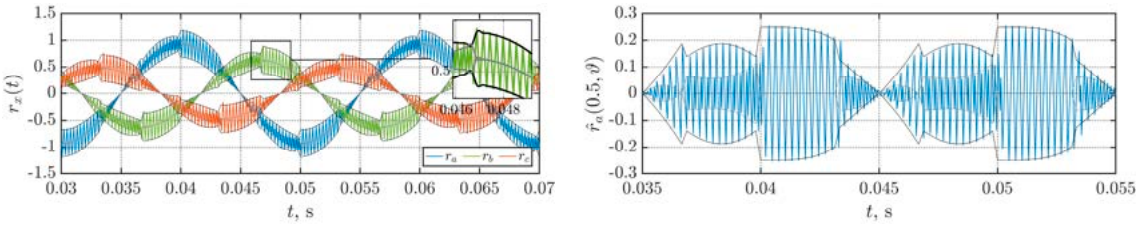

(**a**) (**b**)

Figure 14. Primary (black) and secondary (gray) envelopes in case of DPWM2 at m = 0.5 and f_{sw} = 3.6 kHz: (**a**) Normalized phase currents; (**b**) Normalized phase current ripple.

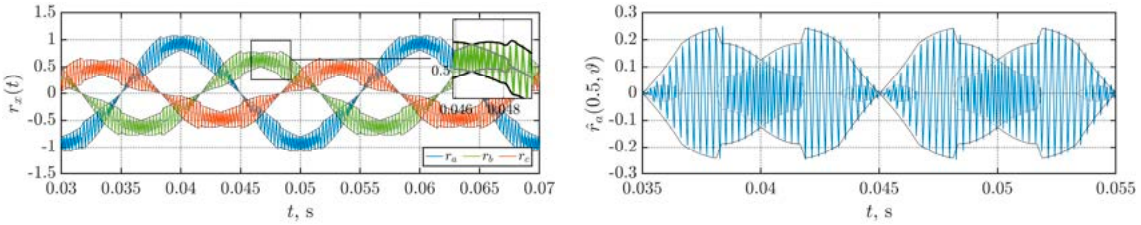

(**a**) (**b**)

Figure 15. Primary (black) and secondary (gray) envelopes in case of DPWM3 at m = 0.5 and f_{sw} = 3.6 kHz: (**a**) Normalized phase currents; (**b**) Normalized phase current ripple.

Current Ripple Peak-to-Peak

By introducing (29) into (3), the primary and secondary normalized peak-to-peak current ripples can be calculated as follows:

$$\begin{cases} \hat{r}'_{a,pp}(t) = u_a(t)\{\text{sign}[u_a(t)] + 2\gamma(t)\} \\ \hat{r}''_{a,pp}(t) = u_a(t)\{-\text{sign}[u_a(t)] + 2u_a(t) + 2\gamma(t)\} \end{cases} \quad (30)$$

In the following pictures, current ripple peak-to-peak as a function of m and ϑ has been depicted for all the considered injections.

As expected, peak-to-peak profiles of SPWM, CPWM, THIPWM1/6, and THIPWM1/4 depicted in Figure 16 have a half-wave symmetry. The secondary peak-to-peak pattern tends to remain confined inside the primary one. Differently from Figure 16, and as discussed before, peak-to-peak profiles of DPWMMAX and DPWMMIN shown in Figure 17 do not present any half-wave symmetry. However, as it has been declared in previous sections, they tend to have a mirrored profile.

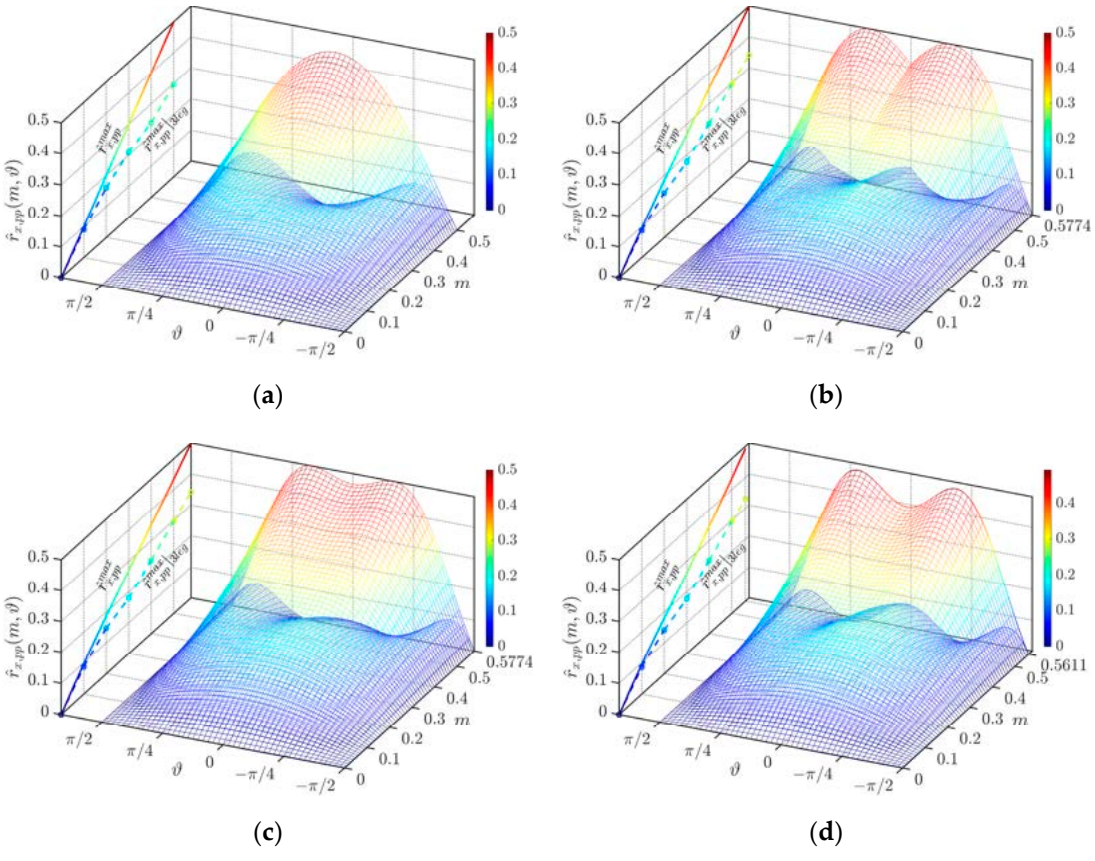

(**a**) (**b**)

(**c**) (**d**)

Figure 16. Normalized primary and secondary peak-to-peak phase current ripples in case of: (**a**) SPWM; (**b**) CPWM; (**c**) THIPWM1/6; and (**d**) THIPWM1/4.

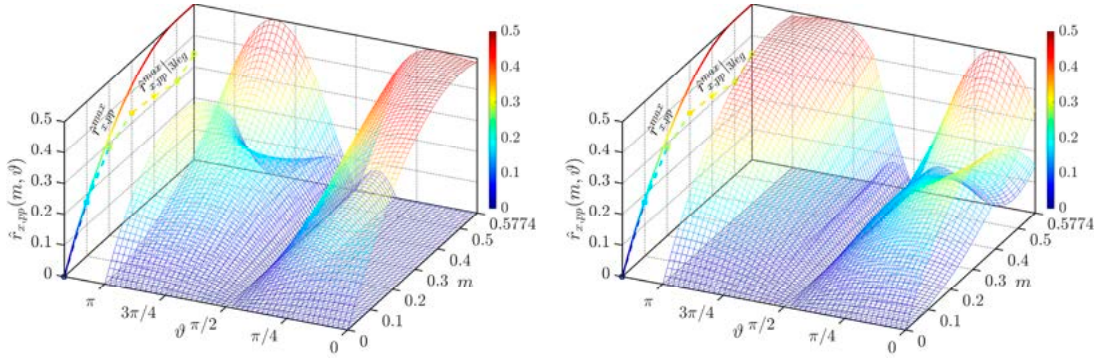

(**a**) (**b**)

Figure 17. Normalized primary and secondary peak-to-peak phase current ripples in case of: (**a**) DPWMMAX; (**b**) DPWMMIN.

Being GDPWM made out of multiple slices of DPWMMAX and DPWMMIN, it can be easily recognized how both primary and secondary peak-to-peak profiles, presented in Figure 18, are the regrouped forms of those depicted in Figure 17.

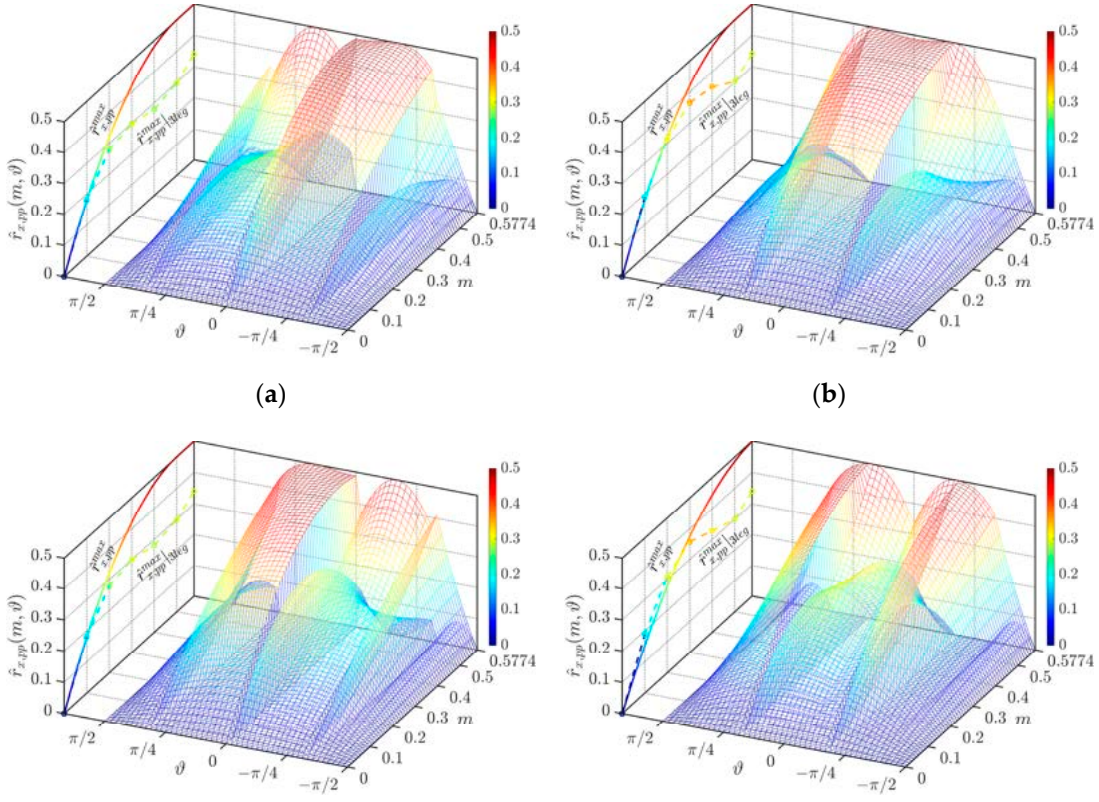

(**a**) (**b**)

(**c**) (**d**)

Figure 18. Normalized primary and secondary peak-to-peak phase current ripples in case of: (**a**) DPWM0; (**b**) DPWM1; (**c**) DPWM2; and (**d**) DPWM3.

Moreover, it can be seen that when a phase is clamped, the term inside of the curly brackets of the secondary peak-to-peak expression in (30) becomes null, leading to the flat, zero profile visible in both Figures 17 and 18. It is also interesting to notice that for lower modulation indices ($m \leq 0.2$) the maximum peak-to-peak values of ac current ripple for the four-leg configuration are pretty close their counterparts from the three-leg VSI (see left 2D axes of Figures 17 and 18). Furthermore, in Figure 18d one can notice slightly better performance of the four-leg VSI over the three-leg one. For the

higher modulation indices ($m > 0.2$), it is well visible that in all of the studied modulation cases, the typical two-level, three-phase VSI configuration ("3leg") outperforms the four-leg VSI architecture, in terms of maximum peak-to-peak current ripple.

Figure 19 displays the normalized maximum peak-to-peak values of the studied injections that have been applied to the four-leg VSI. It can be seen that CPWM, THIPWM1/6 ("THI6"), and THIPWM1/4 ("THI4") behave similarly in the whole m range, always remaining below SPWM trace. All the DPWM injections are presenting worse performance, especially for low m values, if compared with the other counterparts. It can be noticed that DPWMMAX ("DMAX"), DPWMMIN ("DMIN"), DPWM0 ("D0"), DPWM1 ("D1"), and DPWM2 ("D2") share similar behavior. Among the studied here DPWM injections, DPWM3 ("D3") is the one that reveal the best current ripple-related characteristics. Finally, it deserves to be mentioned the fact that as more these injections approach to its linear range m limit, as close one another, their characteristics become (Figure 19b).

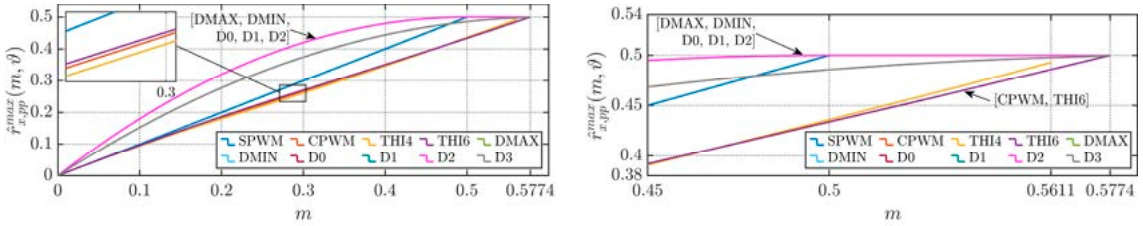

(**a**) (**b**)

Figure 19. (**a**) Normalized maximum peak-to-peak value as a function of m for all the considered injections; (**b**) Magnification for high values of m.

4.2. Phase Current Ripple RMS

From Figure 5, one can notice that voltage pulses can retain only two possible levels. Therefore, all the positive current ramps have the same slope, similarly all negative current ramps have the same steepness. However, it can be easily seen that the ripple waveform in the switching period is not properly triangular.

As done before, for symmetry reasons, it is possible to restrict the study on the right half of the switching period. The current ripple on the right side can be seen as a triangular waveform having a particular offset. Therefore, the rms of the phase current ripple can be determined by separately studying the dc contribution due to the offset and the ac component due to the triangular waveform. The current ripple rms within one switching period can be seen as:

$$\hat{I}_{T_{sw}}(m,\vartheta) = \sqrt{\hat{I}_{T_{sw}}^{dc}(m,\vartheta)^2 + \hat{I}_{T_{sw}}^{ac}(m,\vartheta)^2} \tag{31}$$

where the rms due to the offset can be computed as:

$$\hat{I}_{T_{sw}}^{dc}(m,\vartheta) = \frac{\hat{\imath}'_{pk}(m,\vartheta) + \hat{\imath}''_{pk}(m,\vartheta)}{2} = \frac{V_{dc}}{2Lf_{sw}} \frac{u_x(m,\vartheta)^2 + 2u_x(m,\vartheta)\gamma(m,\vartheta)}{2} \tag{32}$$

Since the alternate component consists of a triangular waveform, its rms can be calculated basing on the crest factor √3 of a triangular waveform as:

$$\hat{I}_{T_{sw}}^{ac}(m,\vartheta) = \frac{\hat{\imath}'_{pk}(m,\vartheta) - \hat{\imath}''_{pk}(m,\vartheta)}{2\sqrt{3}} = \frac{V_{dc}}{2Lf_{sw}} \frac{u_x(m,\vartheta) - u_x(m,\vartheta)^2}{2\sqrt{3}} \tag{33}$$

The total current ripple rms can be obtained by integrating all the rms contributions provided by all the switching cycles within one fundamental period as:

$$\hat{I}(m) = \sqrt{\frac{1}{2\pi}\int_0^{2\pi}\left[\hat{I}_{T_{sw}}(m,\vartheta)\right]^2 d\vartheta} = \sqrt{\frac{1}{2\pi}\int_0^{2\pi}\left[\hat{I}^{dc}_{T_{sw}}(m,\vartheta)^2 + \hat{I}^{ac}_{T_{sw}}(m,\vartheta)^2\right]d\vartheta} \tag{34}$$

Since Equation (33) is injection independent, its contribution is the same for all the modulation strategies.

4.2.1. DPWMMAX and DPWMMIN

As discussed before, the pulses arrangement visible in Figure 5 is valid only from $-\pi/2$ to $\pi/2$, therefore to study DPWMMAX and DPWMMIN rms in whole fundamental period it is necessary for further derivations to employ Equations (15) and (16). Considering modulating signal symmetries, Equation (34) can be rewritten as:

$$\hat{I}(m)^2\big|_{\mathrm{DMAX}} = \frac{1}{2\pi}\int_{-\frac{\pi}{2}}^{\frac{3\pi}{2}} \hat{I}_{T_{sw}}(m,\vartheta)^2\big|_{\mathrm{DMAX}} d\vartheta = \frac{1}{\pi}\int_0^{\frac{\pi}{2}}\left[\hat{I}_{T_{sw}}(m,\vartheta)^2\big|_{\mathrm{DMAX}} + \hat{I}_{T_{sw}}(m,\vartheta)^2\big|_{\mathrm{DMIN}}\right]d\vartheta \tag{35}$$

$$\hat{I}(m)^2\big|_{\mathrm{DMIN}} = \frac{1}{2\pi}\int_{-\frac{\pi}{2}}^{\frac{3\pi}{2}} \hat{I}_{T_{sw}}(m,\vartheta)^2\big|_{\mathrm{DMIN}} d\vartheta = \frac{1}{\pi}\int_0^{\frac{\pi}{2}}\left[\hat{I}_{T_{sw}}(m,\vartheta)^2\big|_{\mathrm{DMAX}} + \hat{I}_{T_{sw}}(m,\vartheta)^2\big|_{\mathrm{DMIN}}\right]d\vartheta \tag{36}$$

which can be further simplified as:

$$\hat{I}(m)^2\big|_{\mathrm{DMAX}} = \hat{I}(m)^2\big|_{\mathrm{DMIN}} = \frac{1}{\pi}\int_0^{\frac{\pi}{2}}\left[\hat{I}^{dc}_{T_{sw}}(m,\vartheta)^2\big|_{\mathrm{DMAX}} + \hat{I}^{dc}_{T_{sw}}(m,\vartheta)^2\big|_{\mathrm{DMIN}} + 2\hat{I}^{ac}_{T_{sw}}(m,\vartheta)^2\right]d\vartheta \tag{37}$$

finally giving:

$$\hat{I}(m)\big|_{\mathrm{DMAX}} = \hat{I}(m)\big|_{\mathrm{DMIN}} = \frac{V_{dc}}{2Lf_{sw}}\frac{m}{2\sqrt{6}}\sqrt{4 - \frac{16+54\sqrt{3}}{3\pi}m + \left(9 + \frac{27\sqrt{3}}{8\pi}\right)m^2} \tag{38}$$

Simulation data points (olive green squares) and analytically derived rms expression (solid trace) displayed in Figure 20 demonstrate the validity of Equation (38) for both DPWMAX and DPWMMIN. All the depicted values were normalized using as a base $V_{dc}/(2Lf_{sw})$ and displayed with symbol R, providing ripple rms functions invariant from system parameters (V_{dc}, L and f_{sw}). Moreover, for lower modulation indices ($m \leq 0.2$) current ripple rms is comparable with the three-leg counterpart (dashed black line in Figure 20). On the other hand, for high modulating index values, the considered four-leg topology is continuously outperformed by the standard three-leg configuration.

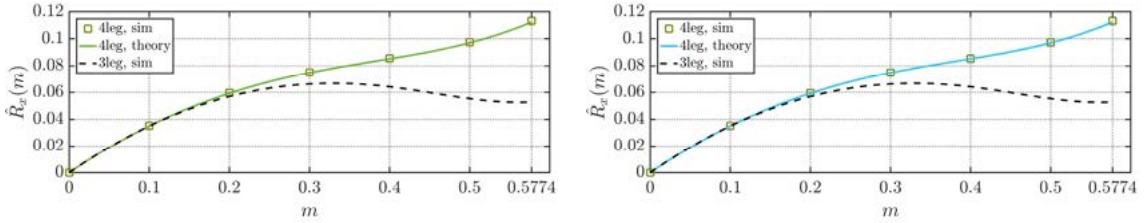

Figure 20. Normalized current ripple rms as a function of m for: (**a**) DPWMMAX; (**b**) DPWMMIN.

4.2.2. DPWM0 and DPWM2

Thanks to the half-wave symmetry of DPWM0 and DPWM2, the rms can be studied within one semi-cycle. Taking advantage of Equations (20) and (22), Equation (34) can be rewritten as:

$$\hat{I}(m)^2\big|_{\mathrm{DPWM0}} = \frac{1}{\pi}\left[\int_{-\frac{\pi}{2}}^{-\frac{\pi}{3}} \hat{I}_{T_{sw}}(m,\vartheta)^2\big|_{\mathrm{DMIN}} d\vartheta + \int_{-\frac{\pi}{3}}^{0} \hat{I}_{T_{sw}}(m,\vartheta)^2\big|_{\mathrm{DMAX}} d\vartheta + \int_{0}^{\frac{\pi}{3}} \hat{I}_{T_{sw}}(m,\vartheta)^2\big|_{\mathrm{DMIN}} d\vartheta + \int_{\frac{\pi}{3}}^{\frac{\pi}{2}} \hat{I}_{T_{sw}}(m,\vartheta)^2\big|_{\mathrm{DMAX}} d\vartheta\right] \tag{39}$$

$$\hat{I}(m)^2\big|_{\mathrm{DPWM2}} = \frac{1}{\pi}\left[\int_{-\frac{\pi}{2}}^{-\frac{\pi}{3}} \hat{I}_{T_{sw}}(m,\vartheta)^2\big|_{\mathrm{DMAX}} d\vartheta + \int_{-\frac{\pi}{3}}^{0} \hat{I}_{T_{sw}}(m,\vartheta)^2\big|_{\mathrm{DMIN}} d\vartheta + \int_{0}^{\frac{\pi}{3}} \hat{I}_{T_{sw}}(m,\vartheta)^2\big|_{\mathrm{DMAX}} d\vartheta + \int_{\frac{\pi}{3}}^{\frac{\pi}{2}} \hat{I}_{T_{sw}}(m,\vartheta)^2\big|_{\mathrm{DMIN}} d\vartheta\right] \tag{40}$$

which for symmetry reasons can be reconducted to:

$$\hat{I}(m)^2\big|_{\mathrm{DPWM0}} = \hat{I}(m)^2\big|_{\mathrm{DPWM2}} = \frac{1}{\pi}\int_{0}^{\frac{\pi}{2}} \left[\hat{I}^{dc}_{T_{sw}}(m,\vartheta)^2\big|_{\mathrm{DMAX}} + \hat{I}^{dc}_{T_{sw}}(m,\vartheta)^2\big|_{\mathrm{DMIN}} + 2\hat{I}^{ac}_{T_{sw}}(m,\vartheta)^2\right] d\vartheta \tag{41}$$

providing the same rms value seen in Equation (38):

$$\hat{I}(m)\big|_{\mathrm{DPWM0}} = \hat{I}(m)\big|_{\mathrm{DPWM2}} = \frac{V_{dc}}{2Lf_{sw}}\frac{m}{2\sqrt{6}}\sqrt{4 - \frac{16+54\sqrt{3}}{3\pi}m + \left(9 + \frac{27\sqrt{3}}{8\pi}\right)m^2} \tag{42}$$

Also for DPWM0 and DPWM2, rms formulations are supported by the simulation data displayed in Figure 21 (normalized using as a base $V_{dc}/(2Lf_{sw})$). Being Equation (42) identical to Equation (38), considerations above can be extended to DPWM0 and DPWM2.

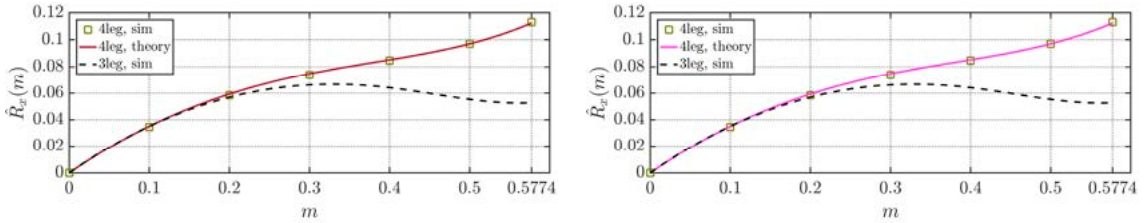

(**a**) (**b**)

Figure 21. Normalized current ripple rms as a function of m for: (**a**) DPWM0; (**b**) DPWM2.

4.2.3. DPWM1

Similarly to what done before, thanks to quarter-wave symmetry and employing Equation (21), relation (34) can be rewritten as:

$$\hat{I}(m)^2\big|_{\mathrm{DPWM1}} = \frac{2}{\pi}\left[\int_{0}^{\frac{\pi}{6}} \hat{I}_{T_{sw}}(m,\vartheta)^2\big|_{\mathrm{DMIN}} d\vartheta + \int_{\frac{\pi}{6}}^{\frac{\pi}{2}} \hat{I}_{T_{sw}}(m,\vartheta)^2\big|_{\mathrm{DMAX}} d\vartheta\right] \tag{43}$$

which can be further simplified as:

$$\hat{I}(m)^2\big|_{\mathrm{DPWM1}} = \frac{2}{\pi}\left[\int_0^{\frac{\pi}{6}} \hat{I}_{T_{sw}}^{dc}(m,\vartheta)^2\big|_{\mathrm{DMIN}} d\vartheta + \int_{\frac{\pi}{6}}^{\frac{\pi}{2}} \hat{I}_{T_{sw}}^{dc}(m,\vartheta)^2\big|_{\mathrm{DMAX}} d\vartheta + \int_0^{\frac{\pi}{2}} \hat{I}_{T_{sw}}^{ac}(m,\vartheta)^2 d\vartheta\right] \tag{44}$$

finally providing the rms expression:

$$\hat{I}(m)\big|_{\mathrm{DPWM1}} = \frac{V_{dc}}{2Lf_{sw}} \frac{m}{2\sqrt{6}} \sqrt{4 - \frac{106}{3\pi} m + \left(9 + \frac{27\sqrt{3}}{12\pi}\right) m^2} \tag{45}$$

The numerical results (normalized using as a base $V_{dc}/(2Lf_{sw})$) of Figure 22a confirm Equation (45).

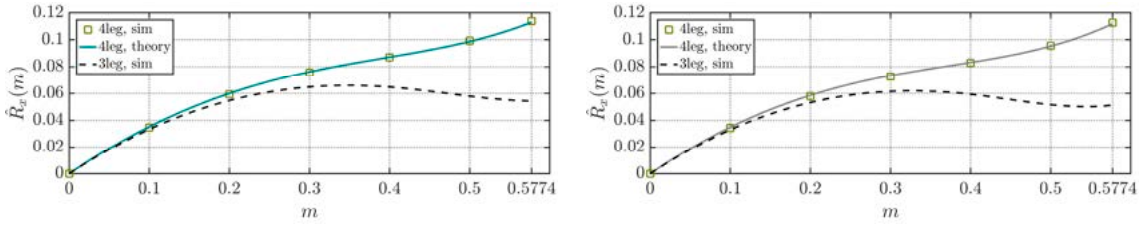

(**a**) (**b**)

Figure 22. Normalized current ripple rms as a function of m for: (**a**) DPWM1; (**b**) DPWM3.

4.2.4. DPWM3

Similarly to what has been done for DPWM1 and employing Equation (24), relation (34) can be rewritten as:

$$\hat{I}(m)^2\big|_{\mathrm{DPWM3}} = \frac{2}{\pi}\left[\int_0^{\frac{\pi}{6}} \hat{I}_{T_{sw}}(m,\vartheta)^2\big|_{\mathrm{DMAX}} d\vartheta + \int_{\frac{\pi}{6}}^{\frac{\pi}{2}} \hat{I}_{T_{sw}}(m,\vartheta)^2\big|_{\mathrm{DMIN}} d\vartheta\right] \tag{46}$$

which can be further simplified as:

$$\hat{I}(m)^2\big|_{\mathrm{DPWM3}} = \frac{2}{\pi}\left[\int_0^{\frac{\pi}{6}} \hat{I}_{T_{sw}}^{dc}(m,\vartheta)^2\big|_{\mathrm{DMAX}} d\vartheta + \int_{\frac{\pi}{6}}^{\frac{\pi}{2}} \hat{I}_{T_{sw}}^{dc}(m,\vartheta)^2\big|_{\mathrm{DMIN}} d\vartheta + \int_0^{\frac{\pi}{2}} \hat{I}_{T_{sw}}^{ac}(m,\vartheta)^2 d\vartheta\right] \tag{47}$$

finally providing the rms function:

$$\hat{I}(m)\big|_{DPWM3} = \frac{V_{dc}}{2Lf_{sw}} \frac{m}{2\sqrt{6}} \sqrt{4 + \frac{74 - 108\sqrt{3}}{3\pi} m + \left(9 + \frac{27\sqrt{3}}{6\pi}\right) m^2} \tag{48}$$

The simulation results (normalized using as a base $V_{dc}/(2Lf_{sw})$) of Figure 22b reasonably match with Equation (48). The classical three-leg rms trace (dashed black line) of Figure 22 outperforms both DPWM1 and DPWM3.

4.2.5. SPWM, CPWM, THIPWM1/6, and THIPWM1/4

For the sake of completeness, here are also reported the rms values for SPWM, CPWM, THIPWM1/6, and THIPWM1/4. Following the same general approach used for the previous modulation cases, it can be demonstrated that the rms functions for the aforementioned continuous modulation strategies are:

$$\hat{I}_x(m_x)\big|_{\mathrm{SPWM}} = \frac{V_{dc}}{2Lf_{sw}} \frac{m_x}{2\sqrt{6}} \sqrt{1 - \frac{16}{3\pi} m_x + 3m_x^2} \tag{49}$$

$$\hat{I}(m)\big|_{\text{CPWM}} = \frac{V_{dc}}{2Lf_{sw}}\frac{m}{2\sqrt{6}}\sqrt{1-\frac{16}{3\pi}m+\left(\frac{9}{2}-\frac{27\sqrt{3}}{8\pi}\right)m^2} \tag{50}$$

$$\hat{I}(m)\big|_{\text{THIPWM1/6}} = \frac{V_{dc}}{2Lf_{sw}}\frac{m}{2\sqrt{6}}\sqrt{1-\frac{16}{3\pi}m+\frac{8}{3}m^2} \tag{51}$$

$$\hat{I}(m)\big|_{\text{THIPWM1/4}} = \frac{V_{dc}}{2Lf_{sw}}\frac{m}{2\sqrt{6}}\sqrt{1-\frac{16}{3\pi}m+\frac{21}{8}m^2} \tag{52}$$

Similar to what has been done above for DPWMs, Figure 23 displays a proper matching between numerical results and analytical findings for SPWM, CPWM, THIPWM1/6, and THIPWM1/4 injections (normalized using as a base $V_{dc}/(2Lf_{sw})$).

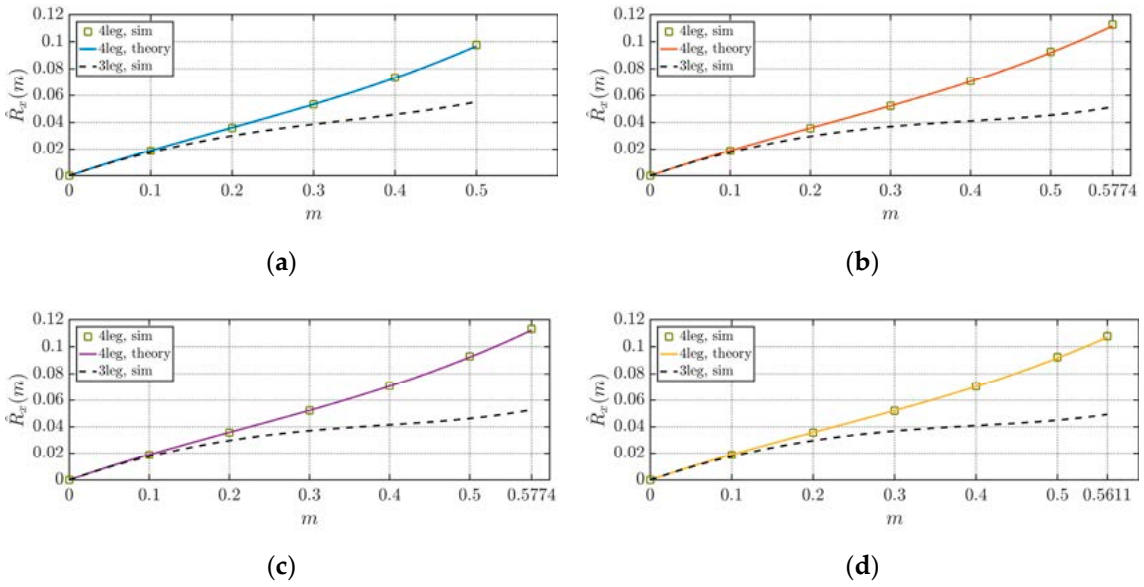

Figure 23. Normalized current ripple rms as a function of m for: (**a**) SPWM; (**b**) CPWM; (**c**) THIPWM1/6; and (**d**) THIPWM1/4.

As visible from Figure 24, DPWMs have worse performance in terms of rms current ripple value within almost whole m range. However, similarly to what was noted for three-leg topology, for high values of m, DPWM profiles approach to the rms values achieved by CPWM making this class of injections particularly suitable in grid-connected applications. Among the DPWM class of injections, DPWM3 is the one presenting the most favorable rms profile.

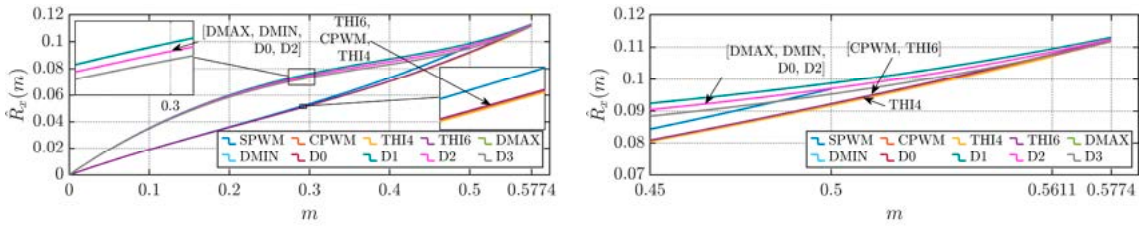

Figure 24. (**a**) Normalized current ripple rms as a function of m for all the considered injections. (**b**) Magnification for high values of m. The normalization base $V_{dc}/(2Lf_{sw})$ has been used.

4.3. Injection Optimization Throughout Frequency Amending

As explained above, the clamping action carried out by DPWMs reduces the number of switching instants, leading to the corresponded reduction of switching losses and optimization of switching frequency. To have a fair comparison between DPWMs and other continuous injections, it is necessary to consider the smaller average switching frequency among compared modulation methods and the lower switching losses by amending the switching frequency.

4.3.1. Average Switching Frequency Compensation

It is well-known that all the DPWM injections share common feature, namely each phase stays clamped for one-third of the fundamental period. In this way, it can be readily stated that the average switching frequency is lower than the one employed in SPWM, CPWM, THIPWM1/6, or THIPWM1/4. As visible in Figure 25a, reducing switching frequency of the CPWM (taken as a benchmark due to its popularity in industrial applications) by a factor 1/3, DPWM peak-to-peak ripple profile has lower values in comparison with the corresponding CPWM (displayed as 3/2CPWM) for $m > 0.21$. Similarly, in Figure 25b, the DPWM3 (best among studied DPWM injections in terms of peak-to-peak and rms current ripple performance) rms current ripple profile starts to provide advantages already for $m > 0.26$ rather than from $m = 0.39$ as it happens in the three-leg counterpart [26]. The same outcome could have been achieved by increasing the DPWM switching frequency by a factor 50%. Finally, it is worth mentioning that for low m values, DPWM behavior comparable with the one shown by CPWM having increased the switching frequency (displayed as 3/2CPWM). For this reason, the DPWM injections result to be particularly suitable in the systems where the current phase angle cannot be easily determined (conversely to what done in the next subsection) regardless of the modulation index considered. Higher rewards are provided for greater values of m, making DPWM class one of the best candidates for grid-connected applications.

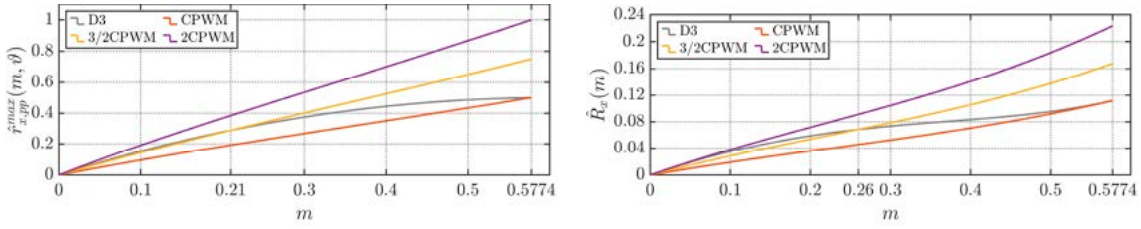

(**a**) (**b**)

Figure 25. DPWM and CPWM compensated comparison of the normalized current ripple: (**a**) maximum peak-to-peak value; (**b**) rms. Average switching frequency compensation is labeled as "3/2 CPWM". Switching losses compensation is marked as "2CPWM". The normalization base $V_{dc}/(2Lf_{sw})$ has been used.

4.3.2. Switching Losses Compensation

Although DPWM techniques share the same principle, they clamp the signals in different regions of the fundamental period. Therefore, different values of phase current in the clamping region create different switching losses. In applications where phase angle φ is known, it is possible to compute the switching losses as [19]:

$$\bar{p}_{sw} = \frac{f_{sw}}{2\pi} k V_{dc} t_{com} \int_0^{2\pi} f(\vartheta)\mathrm{d}\vartheta \quad \text{where} \quad f(\vartheta) = \begin{cases} 0 & |u_a^*(\vartheta)| \geq 0.5 \\ i(\vartheta) = |I_M \cos(\vartheta + \varphi)| & |u_a^*(\vartheta)| < 0.5 \end{cases} \tag{53}$$

where t_{com} represents the commutation duration and k a shape factor usually ranging from 1/6 to 1/2.

Normalizing all the switching losses by considering CPWM losses as a base, it is possible to define the switching losses function (*SLF*) [19]:

$$SLF = \frac{\bar{p}_{sw}}{\bar{p}_{sw}|_{CPWM}} \tag{54}$$

depicted in Figure 26 as function of the phase angle φ.

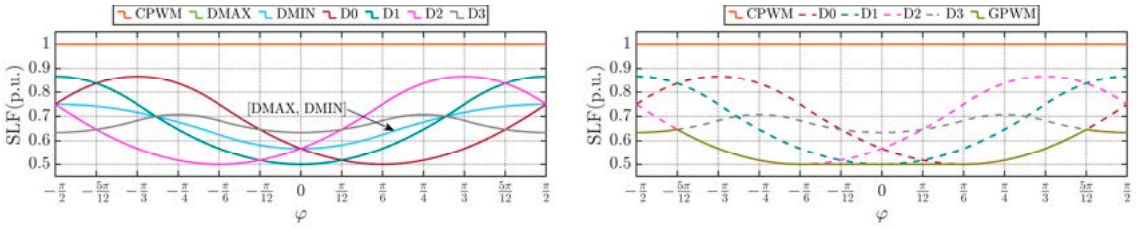

(**a**) (**b**)

Figure 26. Switching loss function in case of: (**a**) CPWM, DPWMMAX, DPWMMIN, DPWM0, DPWM1, DPWM2, and DPWM3; (**b**) Switching loss function in case of optimized GDPWM.

As visible from Figure 26a, DPWM switching losses can be reduced up to half of the CPWM ones. Therefore, one could employ a switching frequency up to two times higher without leading to higher switching losses in comparison with CPWM. Moreover, it can be noticed that DPWMMAX and DPWMMIN have higher *SLF* with respect to at least one of the other DPWM injections in the whole range of phase angle φ. For $|\varphi| \geq 5\pi/12$ (75°), DPWM3 is the one providing the best current ripple behavior. From $-5\pi/12$ to $-\pi/12$ DPWM2 is the best injection in this sense. Similarly, DPWM0 performs better from $\pi/12$ to $5\pi/12$. Finally, within $[-\pi/12; \pi/12]$ range, DPWM1 happens to have the best current ripple characteristics. This switching losses capability has been exploited with the so-called optimized GDPWM (Figure 26b) by setting $\psi_m = \varphi$ in (19) when φ is within $[-\pi/6; \pi/6]$ diapason [19]. In this way, switching losses are halved for power factors above 0.86 and, in general, at least cut by one third for all the remaining phase angles.

As displayed in Figure 25, both DPWM current ripple peak-to-peak and rms characteristics in case of switching losses optimization (CPWM having half switching frequency) outperform similar indicators of CPWM (displayed as 2CPWM) in the whole *m* range. Likewise, the same result could be obtained by doubling the DPWM switching frequency.

Overall, systems in which φ is known can be strongly optimized if DPWM is jointly employed with a switching frequency increment by a factor ranging from 50% to 100%. Especially when cos(φ) > 0.86, peak-to-peak, and rms can be roughly halved although having the same switching losses.

In any case, compensating the sole average switching losses (switching frequency increased by 50%) can provide a good tradeoff between ripple mitigation (about −30%) and lower switching losses. Although DPWM3 is the best injection among the others, from the current ripple performance point of view, GDPWM could provide additional improvement margins if switching losses are compensated (switching frequency increased up to 100%) with ripple diminished by about 50%.

4.3.3. Performance Comparison

Aiming to provide more straightforward comparison in the converter performances under different PWM schemes, a set of Kiviat diagrams (radar/spider-like charts) are depicted in Figure 27. To create the subplots, five metrics have been considered, namely switching frequency (f_{sw}), average switching frequency ($\bar{f}_{sw}$), *SLF*, normalized current ripple rms ($\hat{R}_x$), and normalized maximum current ripple peak-to-peak ($\hat{r}_{x,pp}^{max}$). In this context, unity power factor (φ = 0) and $m = 0.5$ have been considered. In the five depicted subcases, one metric per time has been equalized with the corresponding characteristic of CPWM (SVPWM), for all the injections, permitting to compare the remaining parameters. In Table 1. the five metrics of above are listed considering the same switching frequency for all the injections. Row of Table 1 with CPWM indicators has been used as benchmark. The metrics equalization can be achieved by tuning the switching frequency, as visible from Figure 27b to Figure 27e where $f_{sw} \neq 1$ p.u. Switching frequency and average switching frequency are expressed in p.u. In Figure 27, the aligned characteristics are displayed in red.

Table 1. Same switching frequency performance comparison data for $\varphi = 0$ and $m = 0.5$.

PWM Injection	Label	f_{sw}	$\overline{f}_{sw}$	SLF	$\hat{R}_x$	$\hat{r}_{x,pp}^{max}$
SPWM	SPWM	1	1	1	0.95	0.5
CPWM [1]	CPWM	1	1	1	0.9	0.43
THIPWM1/4	THI4	1	1	1	0.9	0.43
THIPWM1/6	THI6	1	1	1	0.9	0.44
DPWMMAX	DMAX	1	0.(6)	0.57	0.95	0.5
DPWMMIN	DMIN	1	0.(6)	0.57	0.95	0.5
DPWM0	D0	1	0.(6)	0.57	0.95	0.5
DPWM1	D1	1	0.(6)	0.5	0.97	0.5
DPWM2	D2	1	0.(6)	0.57	0.95	0.5
DPWM3	D3	1	0.(6)	0.63	0.93	0.49

[1] CPWM injection assumed as benchmark.

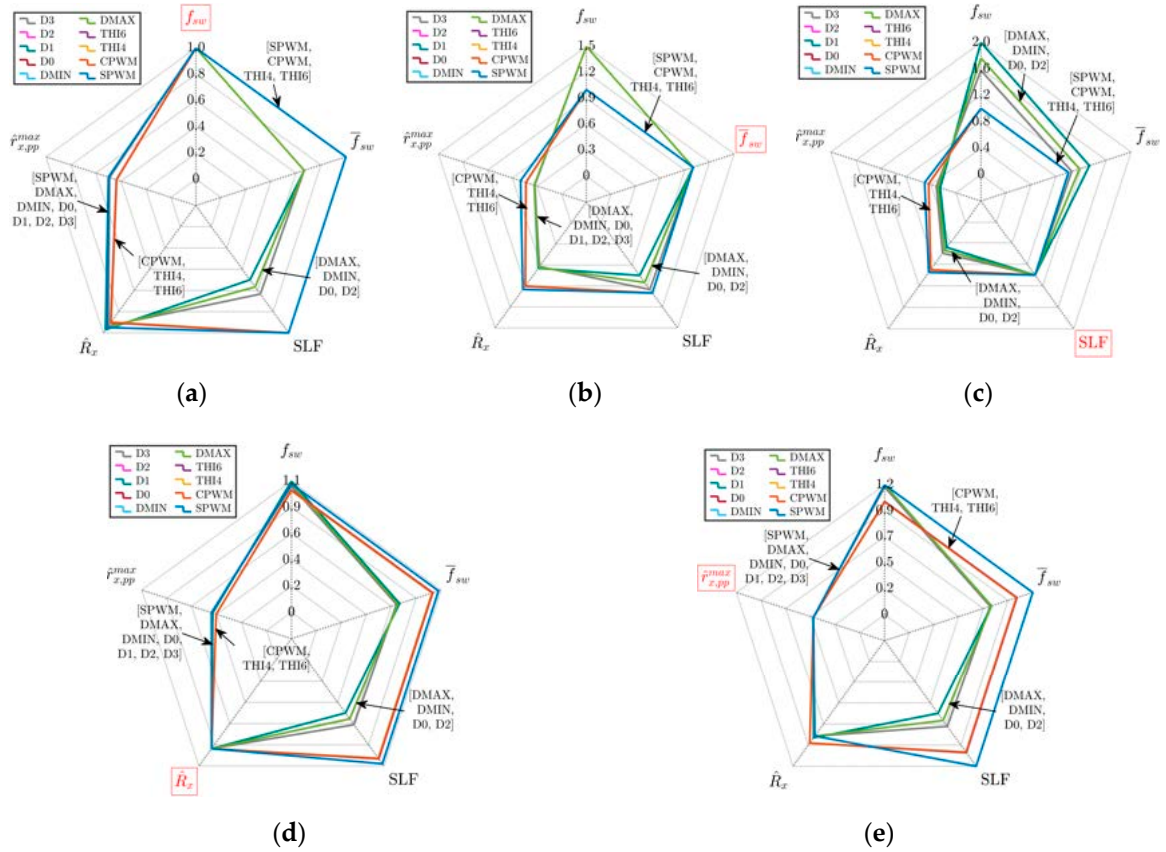

Figure 27. Converter performance comparative Kiviat diagrams at $\varphi = 0$ and $m = 0.5$. Metrics, switching frequency (**a**), average switching frequency (**b**), switching losses function (*SLF*) (**c**), normalized current ripple rms (**d**), and normalized maximum current ripple peak-to-peak (**e**).

In detail, Figure 27a summarizes the data provided in previous sections and collected in Table 1. At the same rate of switching frequency, DPWM injections experience an average switching frequency that is one-third lower and an *SLF* up to two times smaller in comparison with continuous PWMs. At the same time, as previously displayed in Figures 19 and 24, current ripple maximum peak-to-peak and rms are close to one another regardless of which injection is considered.

Furthermore, Figure 27b,c depicts the cases where average switching frequency and commutation losses are compensated by an increase of switching frequency, respectively. As described previously in this section, it is possible to have a relevant improvement in terms of current ripple peak-to-peak and rms (Figure 25) by rising the switching frequency from +50% to +100%

without detrimental effects in the commutation losses. It is worth noticing that compensating the average switching frequency (Figure 27b), the switching losses (*SLF*) employing any method from DPWM class are still below values experienced by the continuous modulations, i.e., SPWM and CPWM.

Finally, in Figure 27d,e, equalized ripple characteristics—maximum peak-to-peak and rms current ripple—are displayed, respectively. Those plots were derived by increasing the switching frequency by a factor that is ranging from 10% to 20%. Again, DPWM injections retain beneficial feature, providing huge switching losses (*SLF*) reduction with respect to CPWM, SPWM, THIPWM1/6, and THIPWM1/4.

The switching frequency variation displayed in Figure 27 suggests that modulation from DPWM class should be employed when dealing with two-level, three-phase, four-leg converters. Overall, switching losses-related metrics (average switching frequency and *SLF*) are sharply improved in the case of DPWM with respect to continuous modulations when the same current ripple rms or maximum peak-to-peak is considered (Figure 27d,e, respectively). On the other hand, setting the same average switching frequency or *SLF* (Figure 27b,c, respectively) ensures a noticeable enhancement in current quality-related metrics (current ripple rms and maximum peak-to-peak).

Thanks to the findings introduced in this section, one could compare performances at different values of modulation index and phase angle, permitting to choose which injection ensures the optimal solution according to given design constraints. This comparison shows the high grade of optimization offered by the considered topology when employed in grid-connected applications. By acting on the switching frequency, optimal tradeoff between switching losses, current ripple performances, power switches technology, filter size and overall cost can be found. As extensively described before, the proposed optimization is possible only when the DPWM class is considered.

5. Analysis of Neutral Current Ripple

Being the neutral current strongly affected by all the phase currents, a generic approach taking into account all possible unbalances results to be cumbersome. As done for the rms, the neutral analysis here presented should be considered valid in a modulation balanced case only. For symmetry reasons, the neutral current ripple waveform shown in Figure 28 is correct only from 0 to $\pi/6$. With respect to balanced modulation, secondary current ripples, present in phase currents, are canceling each other making it equal to zero in the neutral leg current ripple. Therefore, in one half of a switching period, only one peak is present.

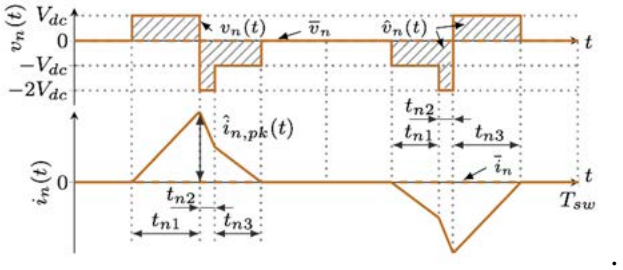

Figure 28. Neutral current ripple waveform (bottom) and equivalent neutral voltage pulse disposition (top) in one switching period.

The equivalent neutral voltage pulse timings are:

$$\begin{cases} t_{n1} = \dfrac{T_{sw}}{2}\left(u_a^*(t) - u_n(t)\right) = \dfrac{T_{sw}}{2}u_a(t) \\ t_{n2} = \dfrac{T_{sw}}{2}\left(u_n(t) - u_b^*(t)\right) = -\dfrac{T_{sw}}{2}u_b(t) \qquad 0 \le \vartheta \le \dfrac{\pi}{6} \\ t_{n3} = \dfrac{T_{sw}}{2}\left(u_b^*(t) - u_c^*(t)\right) = \dfrac{T_{sw}}{2}\left(u_b(t) - u_c(t)\right) \end{cases} \tag{55}$$

From Equation (55) one could already observe that at balanced modulation the neutral current ripple is injection independent.

5.1. Neutral Current Ripple Waveform

Following a similar approach that has been applied in the previous section, neutral current ripple peak can be found from Figure 28 as:

$$\hat{\imath}_{n,pk}(t) = t_{n1}\frac{V_{dc}}{L} = \frac{V_{dc}}{2Lf_{sw}}u_a(t) \quad 0 \le \vartheta \le \frac{\pi}{6} \tag{56}$$

that if inserted in Equation (3) and normalized with $V_{dc}/(2Lf_{sw})$ gives the simple peak-to-peak expression:

$$\hat{r}_{n,pp}(t) = 2u_a(t) = 2m_a\cos(\vartheta) \quad 0 \le \vartheta \le \frac{\pi}{6} \tag{57}$$

Similarly, the possibility of wrapping an unbalanced neutral current (at balanced modulation) is verified in Figure 29a. The resulting neutral current is generated by the set of phase currents shown in Section 4. Likewise, in Figure 29b, the neutral current ripple is depicted. As it is well visible, the only significant envelope is the primary one of (56). Overall, the analytically derived expressions of neutral current ripple envelopes (normalized using the base $V_{dc}/(2Lf_{sw})$) nicely match with the simulation results, depicted in Figure 29.

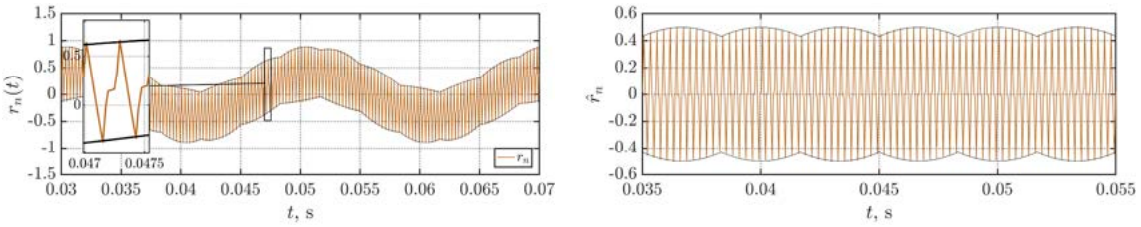

(**a**) (**b**)

Figure 29. Profile and primary (black) envelope in case of m = 0.5 and f_{sw} = 3.6 kHz: (**a**) Normalized neutral current; (**b**) Normalized neutral current ripple.

By comparing Figures 5 and 28 it is well visible that the time instances of neutral ripple peaks correspond to the exactly the same moments when primary peaks of phase current ripples appear. The latter ones always happen at the neutral leg switching instances, therefore, a generic relation of neutral peak-to-peak current ripple can be found. By a straightforward summation of phase peak-to-peak current ripple functions, it is possible obtain the neutral current peak-to-peak expression that is valid in the whole fundamental period as:

$$\hat{r}_{n,pp}(t) = \sum_{x=a,b,c}\hat{r}_{x,pp}(t) \tag{58}$$

which can be rewritten as:

$$\hat{r}_{n,pp}(t) = \pm[|u_a(t)| + |u_b(t)| + |u_c(t)|] + \gamma(t)[u_a(t) + u_b(t) + u_c(t)] \tag{59}$$

that in the case of SPWM (γ(t) = 0) or balanced modulation gives the injection invariant relation (for this reason only one ripple profile has been depicted in this section):

$$\hat{r}_{n,pp}(t) = \pm[|u_a(t)| + |u_b(t)| + |u_c(t)|] \tag{60}$$

It should be mentioned that in the case of SPWM, Equation (60) is also valid for unbalanced modulations.

Moreover, in case of the balanced modulation only, Equation (60) can be rewritten as:

$$\hat{r}_{n,pp}(t) = \pm 2\max[u_a(\vartheta), u_b(\vartheta), u_c(\vartheta)] \tag{61}$$

that if restricted in the interval [0, π/6] becomes equal to Equation (57). Figure 30 represents Equation (57) in a graphical way as a function of both ϑ and m.

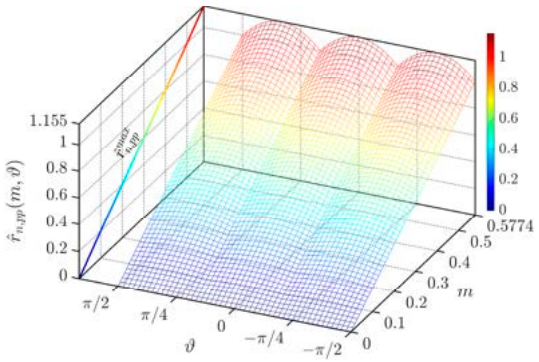

Figure 30. Normalized primary peak-to-peak neutral current ripple profile.

5.2. Neutral Current Ripple RMS

Differently from what has been done in the previous section with phase currents, it is not possible to take advantage of the current ripple triangular-like waveform. However, by considering each interval t_{nk} as a sawtooth function, the ripple calculation approach presented before can be employed as well. In particular, by modifying Equation (31) as:

$$\hat{I}_{n,T_{sw}}(m,\vartheta) = \sqrt{\frac{2}{T_{sw}}\sum_{k=1}^{3} t_{nk}\left[\hat{I}_{t_{nk}}^{dc}(m,\vartheta)^2 + \hat{I}_{t_{nk}}^{ac}(m,\vartheta)^2\right]} \tag{62}$$

one can eventually obtain:

$$\hat{I}_n(m) = \sqrt{\frac{6}{\pi}\int_0^{\frac{\pi}{6}}\left[\hat{I}_{n,T_{sw}}(m,\vartheta)\right]^2 d\vartheta} = \frac{V_{dc}}{2Lf_{sw}}\sqrt{m^3}\sqrt{\frac{2\sqrt{3}-2}{\pi}} \tag{63}$$

Equation (63) can be normalized as:

$$\hat{R}_n(m) = \sqrt{m^3}\sqrt{\frac{2\sqrt{3}-2}{\pi}} \tag{64}$$

Equation (64) results to be valid for computing the neutral current ripple rms in balanced modulation regardless of the injection considered. An approximated version was already available in [27]. Equation (64) perfectly matches with the numerical result presented in Figure 31 by olive green squares.

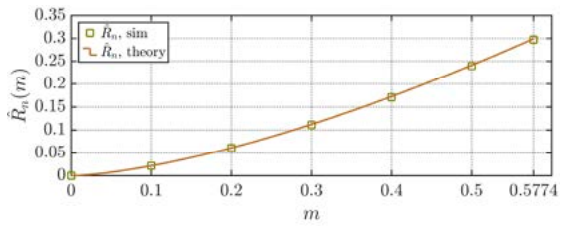

Figure 31. Normalized neutral current ripple rms as a function of m.

6. Experimental Results

In this section, experimental results are presented to support analytical claims provided in this paper for all the considered PWM injections. The experimental setup, given in Figure 32a, consists of the four-leg VSI topology (see Figure 1) connected to the three-phase load depicted in Figure 32b.

This *RLC* topology permits to emulate a unity power factor, grid-connected system. (the same rule applies to IEEE Transaction journals).

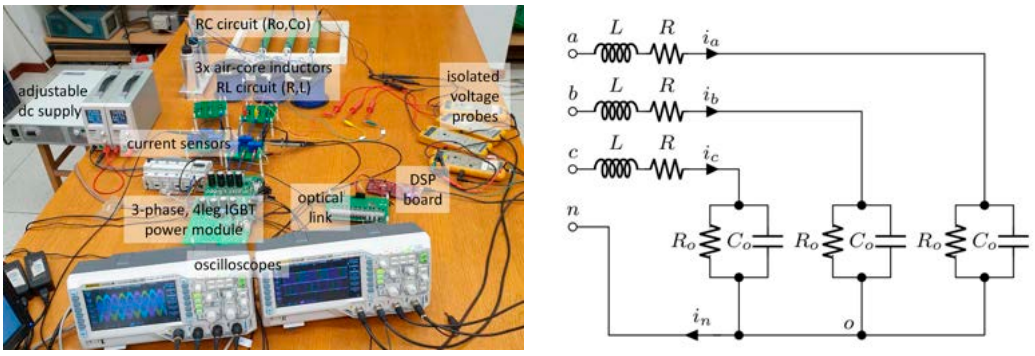

(**a**) (**b**)

Figure 32. (**a**) Experimental laboratory workbench; (**b**) Unitary power factor load.

Overall the setup is made out of a four-leg VSI, employing two standard three-phase insulated-gate bipolar transistor (IGBT) power modules (PS22A76, 1200V, 25A, Mitsubishi Electric Corporation, Tokyo, Japan) and supplied by an adjustable dc supply (GEN100-33, 100V, 33A, TDK-Lambda Corporation, Tokyo, Japan). The series *RL* circuit is made of three magnetically independent air-core inductors. Meanwhile, the *RC* circuit utilizes a parallel connection of an ac capacitor and a resistor for each of the three phases. Circuital parameters are summarized in Table 2. The switching frequency that has been used in the experiments was selected so low on purpose to display ripple profiles more evidently. Phase and neutral currents are sensed by mean of Hall effect-based current transducers (LA 55-P, 55A, LEM Europe GmbH, Fribourg, Switzerland). Phase voltages are measured through differential isolated voltage probes (PICO TS057, Tyler, TX, USA). The VSI is driven by the digital signal processor (DSP) board (TMS320 F28379D, Texas Instruments, Dallas, TX, USA) via decoupling optical links. The DSP software is deployed via MATLAB/Simulink (MathWorks, Natick, MA, USA) platform in external mode, ensuring the real-time control of all the variables. The experimental datapoints were acquired using two digital oscilloscopes (DS1054Z, Rigol, Beijing, China) at a sampling rate of 5 MHz (without filtering action) and post-processed (plotted) via MATLAB.

Table 2. Experimental setup circuital parameters.

Parameter	Symbol	Value	Unit
dc link voltage	V_{dc}	100	V
RL circuit	R	727	mΩ
	L	1.73	mH
RC circuit	R_o	6.6	Ω
	C_o	45	μF
Power factor @50Hz	PF	1	-
Switching frequency	f_{sw}	3.6	kHz

Phase and neutral currents have been acquired using exactly the same setup but changing only the type of common-mode injection considered. In all the cases, a balanced modulation has been considered.

From Figures 33–42, experimental phase currents, and the corresponding current ripple rms has been displayed. Subfigures labeled as "(a)" represent the currents at the highest modulation index available for the considered modulation. Subplots with a label "(b)" depict current ripple rms for phase *b* in the whole linear modulation range. It is evident from the figures that both primary and secondary envelopes correctly bond the phase current profiles for all implemented injections. The same observation can be done with the current ripple rms values (olive green circles in Figures 33b–

42b) that were experimentally obtained with reasonable discretization of modulation range for all the studied injections.

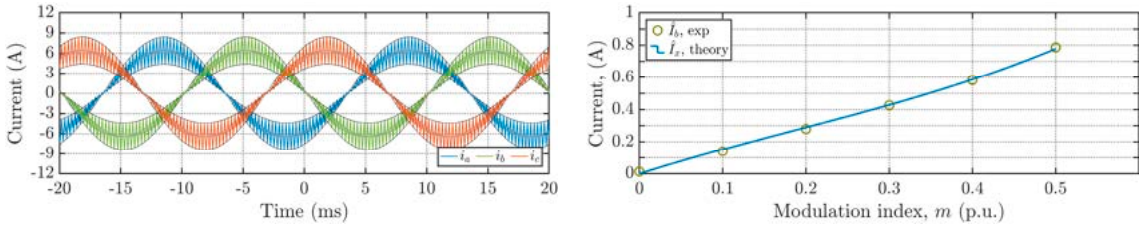

(**a**) (**b**)

Figure 33. (**a**) Phase currents with primary (black) and secondary (gray) envelopes in case of SPWM (m = 0.5); (**b**) Phase current ripple rms in case of SPWM.

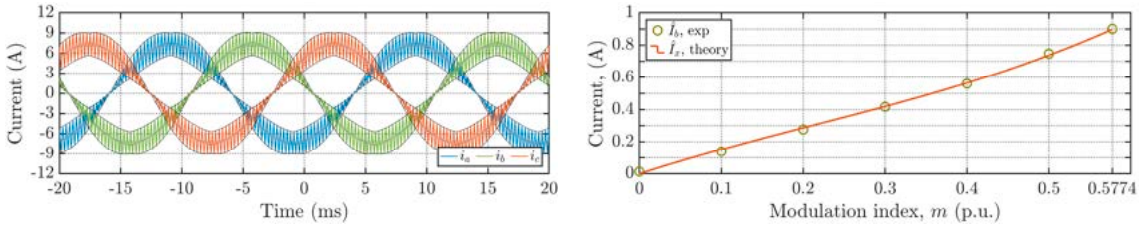

(**a**) (**b**)

Figure 34. (**a**) Phase currents with primary (black) and secondary (gray) envelopes in case of CPWM (m = 1/√3); (**b**) Phase current ripple rms in case of CPWM.

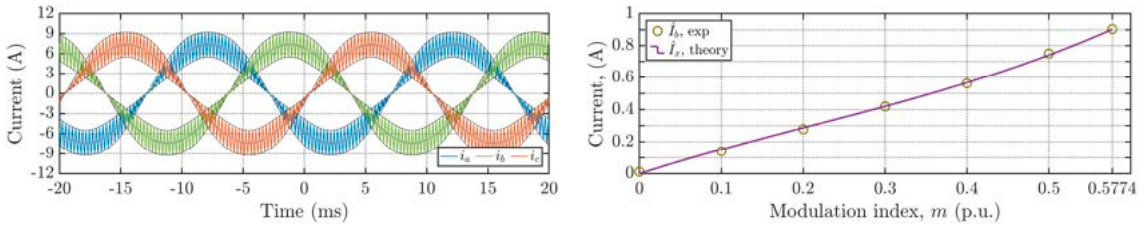

(**a**) (**b**)

Figure 35. (**a**) Phase currents with primary (black) and secondary (gray) envelopes in case of THIPWM1/6 (m = 1/√3); (**b**) Phase current ripple rms in case of THIPWM1/6.

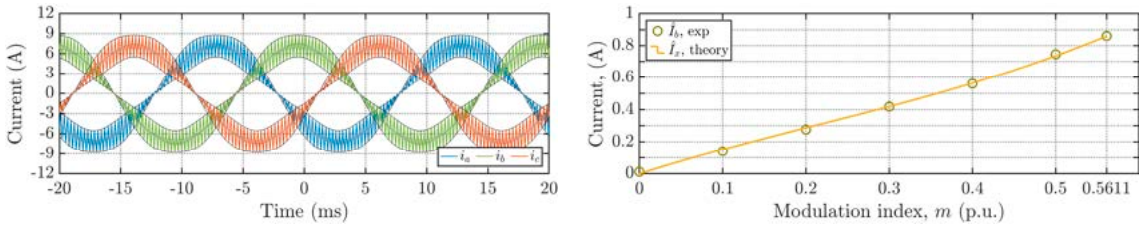

(**a**) (**b**)

Figure 36. (**a**) Phase currents with primary (black) and secondary (gray) envelopes in case of THIPWM1/4 (m = 6√3/(7√7)); (**b**) Phase current ripple rms in case of THIPWM1/4.

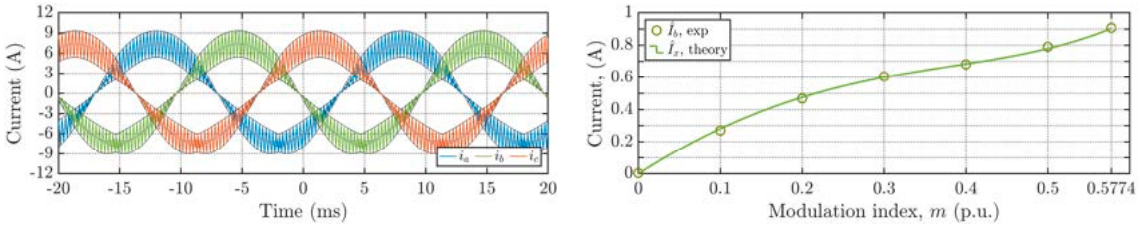

(**a**) (**b**)

Figure 37. (**a**) Phase currents with primary (black) and secondary (gray) envelopes in case of DPWMMAX ($m = 1/\sqrt{3}$); (**b**) Phase current ripple rms in case of DPWMMAX.

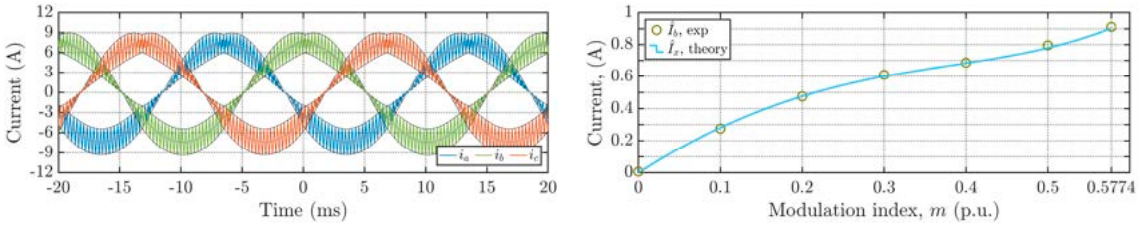

(**a**) (**b**)

Figure 38. (**a**) Phase currents with primary (black) and secondary (gray) envelopes in case of DPWMMIN ($m = 1/\sqrt{3}$); (**b**) Phase current ripple rms in case of DPWMMIN.

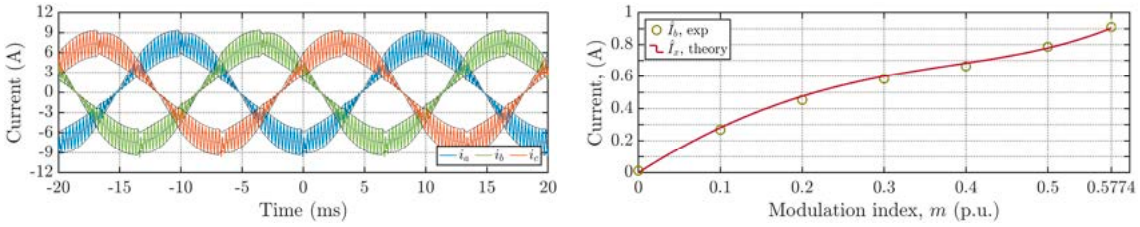

(**a**) (**b**)

Figure 39. (**a**) Phase currents with primary (black) and secondary (gray) envelopes in case of DPWM0 ($m = 1/\sqrt{3}$); (**b**) Phase current ripple rms in case of DPWM0.

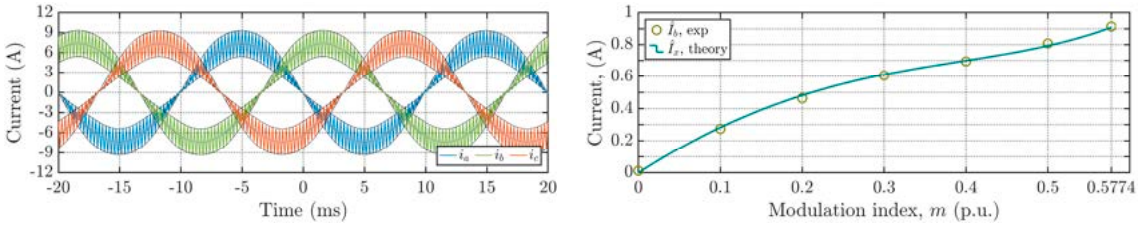

(**a**) (**b**)

Figure 40. (**a**) Phase currents with primary (black) and secondary (gray) envelopes in case of DPWM1 ($m = 1/\sqrt{3}$); (**b**) Phase current ripple rms in case of DPWM1.

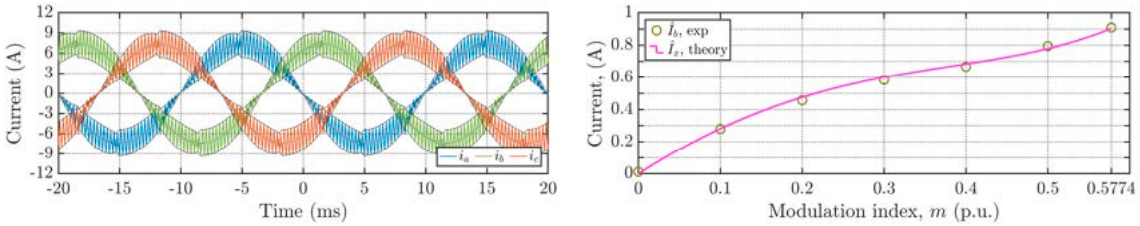

(**a**) (**b**)

Figure 41. (**a**) Phase currents with primary (black) and secondary (gray) envelopes in case of DPWM2 ($m = 1/\sqrt{3}$); (**b**) Phase current ripple rms in case of DPWM2.

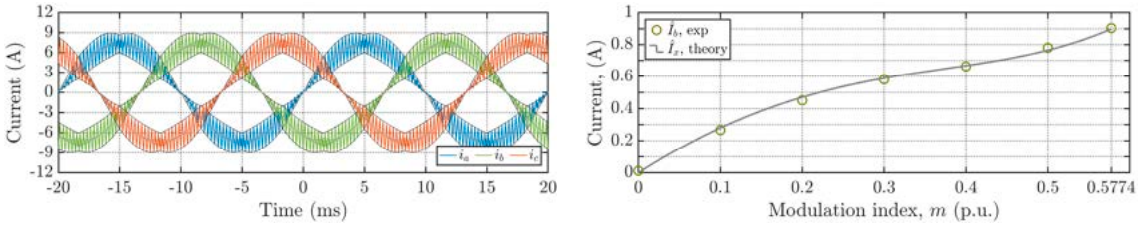

(**a**) (**b**)

Figure 42. (**a**) Phase currents with primary (black) and secondary (gray) envelopes in case of DPWM3 ($m = 1/\sqrt{3}$); (**b**) Phase current ripple rms in case of DPWM3.

Since the three-phase load is balanced and the modulating scheme is symmetric, neutral wire experiences the ripple component only. Therefore the neutral current depicted in Figure 43a happens to be equal to the neutral current ripple itself. Also for the neutral current, both envelopes (Figure 43a) and rms values (Figure 43b) are validated through experimental results. For the sake of completeness, it should be mentioned that the case of Figure 43 represents a DPWMMAX injection. Nevertheless, as it has been verified that in all the analyzed modulations, neutral current ripple characteristics are injection invariant (balanced modulation only), thus, Figure 43 is valid for the other modulation methods.

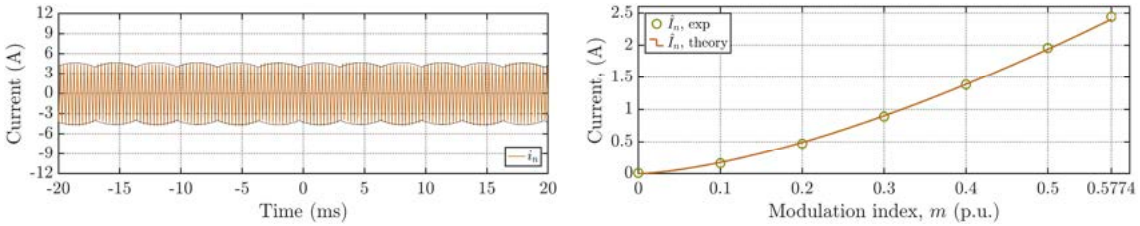

(**a**) (**b**)

Figure 43. (**a**) Neutral current with primary (black) envelope ($m = 1/\sqrt{3}$); (**b**) Neutral current ripple rms.

7. Conclusions

This paper provides a detailed analysis of the switching ac current ripple in three-phase, four-leg inverters employing the most popular PWM common-mode injections. Both phase and neutral currents ripple characteristics have been analyzed in detail.

Firstly, generalized expressions of phase current ripple envelopes and peak-to-peak phase currents are provided in the whole fundamental period as a function of modulation index and phase angle. Moreover, an accurate phase current ripple rms expression as a function of the modulation index has been also derived for all the considered injections. It has been verified that DPWM performances in terms of current ripple and for high values of modulation index approach to the

ones of SPWM and CPWM (SVPWM). Similarly to the traditional three-phase inverter, it has been verified that DPWM1 is the worst injection within analyzed from DPWM class. Meanwhile, DPWM3 is the one ensuring the best current ripple performances.

Furthermore, neutral current ripple indicators have been discussed as well in this paper. It has been demonstrated that the neutral current ripple profile is independent of common-mode injections in the case of balanced modulation/voltages. Both envelopes and peak-to-peak expressions have been determined in the whole fundamental cycle as a function of modulation index and phase angle. Likewise, neutral current ripple rms have been derived as a function of modulation index.

Finally, a fair comparison of continuous and discontinuous modulations was provided by fixing one of the five parameters at the constant value, namely switching frequency, average switching frequency, switching losses, normalized current ripple rms and normalized maximum peak-to-peak current ripple, while compare the rest. It has been proven that average switching frequency equalization (by using a switching frequency 50% higher) is an effective way to improve converter performances when the power factor is unknown. Applications with well-defined phase angle might still take advantage of this analysis for better utilization of the converter capabilities tuning the switching frequency (up to two times higher) for having same switching losses. In this context, it has been demonstrated that DPWM class outperforms other common-mode injections.

Classical three-leg, three-wire inverter characteristics have been indicated as a reference point. In all the modulation cases, both peak-to-peak and rms values are practically doubled in the case of four-leg inverter. Therefore, the four-leg topology should be considered only when it is applied in systems with unbalanced currents and presence of neutral wire is necessary. In case of standard three-phase, three-wire applications the neutral leg should be turned off.

All analytical developments have been verified employing extensive numerical simulations and experimental measurement, for both phase and neutral current ripples and for every considered modulation schemes. All in all, the excellent matching among theoretical findings, simulation and experimental results has validated the given analysis accuracy and effectiveness.

Overall, it has been shown that, if possible, DPWM with properly tuned switching frequency strategies should be preferred because able to guarantee strongly improved current ripple characteristics (from −30% to −50% of the magnitude of related ripple indicator obtained by CPWM scheme), without introducing detrimental effects on the switching losses and, therefore, on the total inverter efficiency. Alternatively, one could halve the switching losses without effecting output current quality. Moreover, this analysis permits optimization for the design of four-leg converters finding the optimal tradeoff between switching losses, current ripple characteristics, switching frequency, power switches technology, filter size, and overall cost. Additional studies could extend the current analysis for other modulation schemes and considering generic unbalances.

Author Contributions: Conceptualization, R.M., A.V., M.H., M.R., and G.G.; methodology, R.M., M.R., and G.G.; software, R.M. and A.V.; validation, R.M., A.V., and M.H.; formal analysis, R.M. and G.G.; investigation, R.M. and G.G.; resources, R.M., A.V., and M.H.; data curation, A.V.; writing—original draft preparation, R.M., A.V. and M.H.; writing—review and editing, R.M., A.V., M.H., M.R., and G.G.; visualization, R.M. and A.V.; supervision, M.R. and G.G. All authors have read and agreed to the published version of the manuscript.

Funding: This research received no external funding.

Conflicts of Interest: The authors declare no conflict of interest.

References

1. De Freitas, T.M.H.; da Silva, S.A.O.; Sampaio, L.P. Dynamic performance comparison involving grid-connected PV systems operating with active power-line conditioning and subjected to sudden solar irradiation changes. *IET Renew. Power Gener.* **2019**, *13*, 587–597, doi:10.1049/iet-rpg.2018.5810.
2. Carrasco, G.; Silva, C.A.; Pena, R.; Cardenas, R. Control of a Four-Leg Converter for the Operation of a DFIG Feeding Stand-Alone Unbalanced Loads. *IEEE Trans. Ind. Electron.* **2015**, *62*, 4630–4640, doi:10.1109/TIE.2014.2364155.

3. Yaramasu, V.; Rivera, M.; Wu, B.; Rodriguez, J. Model Predictive Current Control of Two-Level Four-Leg Inverters—Part I: Concept, Algorithm, and Simulation Analysis. *IEEE Trans. Power Electron.* **2013**, *28*, 3459–3468, doi:10.1109/TPEL.2012.2227509.
4. Rivera, M.; Yaramasu, V.; Rodriguez, J.; Wu, B. Model Predictive Current Control of Two-Level Four-Leg Inverters—Part II: Experimental Implementation and Validation. *IEEE Trans. Power Electron.* **2013**, *28*, 3469–3478, doi:10.1109/TPEL.2012.2227825.
5. Khadkikar, V.; Chandra, A.; Singh, B. Digital signal processor implementation and performance evaluation of split capacitor, four-leg and three H-bridge-based three-phase four-wire shunt active filters. *IET Power Electron.* **2011**, *4*, 463, doi:10.1049/iet-pel.2010.0198.
6. Viatkin, A.; Hammami, M.; Grandi, G.; Ricco, M. Analysis of a Three-Phase Four-Leg Front-End Converter for EV Chargers with Balanced and Unbalanced Grid Currents. In Proceedings of the IECON 2019—45th Annual Conference of the IEEE Industrial Electronics Society, Lisbon, Portugal, 14–17 October 2019; pp. 3442–3449.
7. Lin, Z.; Ruan, X.; Jia, L.; Zhao, W.; Liu, H.; Rao, P. Optimized Design of the Neutral Inductor and Filter Inductors in Three-Phase Four-Wire Inverter with Split DC-Link Capacitors. *IEEE Trans. Power Electron.* **2019**, *34*, 247–262, doi:10.1109/TPEL.2018.2812278.
8. Nascimento, C.F.; Diene, O.; Watanabe, E.H. Analytical model of three-phase four-wire VSC operating as grid forming power converter under unbalanced load conditions. In Proceedings of the 2017 IEEE 12th International Conference on Power Electronics and Drive Systems (PEDS), Honolulu, HI, USA, 12–15 December 2017; pp. 1219–1224.
9. Hintz, A.; Prasanna, R.; Rajashekara, K. Comparative study of three-phase grid connected inverter sharing unbalanced three-phase and/or single-phase systems. In Proceedings of the 2015 IEEE Energy Conversion Congress and Exposition (ECCE), Montreal, QC, Canada, 20–24 September 2015; pp. 6491–6496.
10. Zhao, W.; Ruan, X.; Yang, D.; Chen, X.; Jia, L. Neutral Point Voltage Ripple Suppression for a Three-Phase Four-Wire Inverter with an Independently Controlled Neutral Module. *IEEE Trans. Ind. Electron.* **2017**, *64*, 2608–2619, doi:10.1109/TIE.2016.2632678.
11. Hava, A.M.; Kerkman, R.J.; Lipo, T.A. Carrier-Based PWM-VSI overmodulation strategies: Analysis, comparison, and design. *IEEE Trans. Power Electron.* **1998**, *13*, 674–689, doi:10.1109/63.704136.
12. Hava, A.M.; Kerkman, R.J.; Lipo, T.A. Simple analytical and graphical methods for carrier-based PWM-VSI drives. *IEEE Trans. Power Electron.* **1999**, *14*, 49–61, doi:10.1109/63.737592.
13. Holmes, D.G.; Lipo, T.A. *Pulse Width Modulation for Power Converters: Principles and Practice*; John Wiley & Sons: Hoboken, NJ, USA, 2003; ISBN 9780470546284.
14. Holtz, J. Pulsewidth Modulation for Electronic Power Conversion. *Proc. IEEE* **1994**, *82*, 1194–1214, doi:10.1109/5.301684.
15. Depenbrock, M. Pulse width control of a 3-phase inverter with non-sinusoidal phase voltages. In *Conference Record of IEEE/IAS Annual Meeting*; IEEE: New York, NY, USA, 1977; pp. 399–403.
16. Ogasawara, S.; Akagi, H.; Nabae, A. A novel PWM scheme of voltage source inverters based on space vector theory. *Arch. Elektrotech.* **1990**, *74*, 33–41, doi:10.1007/BF01573229.
17. Kolar, J.W.; Ertl, H.; Zach, F.C. Influence of the modulation method on the conduction and switching losses of a PWM converter system. *IEEE Trans. Ind. Appl.* **1991**, *27*, 1063–1075, doi:10.1109/28.108456.
18. Ojo, O. The Generalized Discontinuous PWM Scheme for Three-Phase Voltage Source Inverters. *IEEE Trans. Ind. Electron.* **2004**, *51*, 1280–1289, doi:10.1109/TIE.2004.837919.
19. Hava, A.M.; Kerkman, R.J.; Lipo, T.A. A high-performance generalized discontinuous PWM algorithm. *IEEE Trans. Ind. Appl.* **1998**, *34*, 1059–1071, doi:10.1109/28.720446.
20. An, S.; Sun, X.; Zhong, Y.; Matsui, M. Research on a new and generalized method of discontinuous PWM strategies to minimize the switching loss. In Proceedings of the IEEE PES Innovative Smart Grid Technologies, Tianjin, China, 21–24 May 2012; pp. 1–6.
21. Grandi, G.; Loncarski, J.; Seebacher, R. Effects of current ripple on dead-time distortion in three-phase voltage source inverters. In Proceedings of the 2012 IEEE International Energy Conference and Exhibition (ENERGYCON), Florence, Italy, 9–12 September 2012; pp. 207–212.
22. Wu, F.; Feng, F.; Luo, L.; Duan, J.; Sun, L. Sampling period online adjusting-based hysteresis current control without band with constant switching frequency. *IEEE Trans. Ind. Electron.* **2015**, *62*, 270–277, doi:10.1109/TIE.2014.2326992.

23. Jiang, D.; Wang, F. Variable Switching Frequency PWM for Three-Phase Converters Based on Current Ripple Prediction. *IEEE Trans. Power Electron.* **2013**, *28*, 4951–4961, doi:10.1109/TPEL.2013.2240701.
24. Grandi, G.; Loncarski, J. Evaluation of current ripple amplitude in three-phase PWM voltage source inverters. In Proceedings of the 2013 International Conference-Workshop Compatibility and Power Electronics, Ljubljana, Slovenia, 5–7 June 2013; pp. 156–161.
25. Grandi, G.; Loncarski, J.; Dordevic, O. Analysis and Comparison of Peak-to-Peak Current Ripple in Two-Level and Multilevel PWM Inverters. *IEEE Trans. Ind. Electron.* **2015**, *62*, 2721–2730, doi:10.1109/TIE.2014.2363624.
26. Grandi, G.; Loncarski, J.; Srndovic, M. Analysis and Minimization of Output Current Ripple for Discontinuous Pulse-Width Modulation Techniques in Three-Phase Inverters. *Energies* **2016**, *9*, 380, doi:10.3390/en9050380.
27. Viatkin, A.; Mandrioli, R.; Hammami, M.; Ricco, M.; Grandi, G. Theoretical Analysis of the AC Current Ripple in Three-Phase Four-Leg Sinusoidal PWM Inverters. In Proceedings of the 2020 IEEE 29th International Symposium on Industrial Electronics (ISIE), Delft, Netherlands, 17–19 June 2020; pp. 796–801.
28. Hou, C.; Wang, P.; Chen, C.; Chang, C. Common Mode Voltage Reduction in Four-Leg Inverter with Multicarrier PWM Scheme. In Proceedings of the 2019 10th International Conference on Power Electronics and ECCE Asia (ICPE 2019—ECCE Asia), Busan, Korea (South), 27–30 May 2019; pp. 3223–3228.
29. Bouarfa, A.; Bodson, M.; Fadel, M. An Optimization Formulation of Converter Control and Its General Solution for the Four-Leg Two-Level Inverter. *IEEE Trans. Control Syst. Technol.* **2018**, *26*, 1901–1908, doi:10.1109/TCST.2017.2738608.
30. Cai, W.; Shen, Y.; Xiao, X.; Wang, W.; Zhang, W.; Li, K.; Zhang, C.; Zhao, Z. Design of the Neutral Line Inductor for Three-phase Four-leg Inverters. In Proceedings of the 2019 IEEE Sustainable Power and Energy Conference (iSPEC), Beijing China, 21–23 November 2019; pp. 2455–2460.